

1 **Estimating the lateral transfer of organic carbon through the European river**  
2 **network using a land surface model**

3 Haicheng Zhang<sup>1\*</sup>, Ronny Lauerwald<sup>2</sup>, Pierre Regnier<sup>1</sup>, Philippe Ciais<sup>3</sup>, Kristof Van Oost<sup>4</sup>,  
4 Victoria Naipal<sup>5</sup>, Bertrand Guenet<sup>3</sup>, Wenping Yuan<sup>6</sup>

5 <sup>1</sup>Department Geoscience, Environment & Society-BGEOSYS, Université libre de Bruxelles, 1050 Bruxelles,  
6 Belgium

7 <sup>2</sup> Université Paris-Saclay, INRAE, AgroParisTech, UMR ECOSYS, 78850, Thiverval-Grignon, France

8 <sup>3</sup>Laboratoire des Sciences du Climat et de l'Environnement, IPSL-LSCE CEA/CNRS/UVSQ, Orme des Merisiers,  
9 91191, Gif sur Yvette, France

10 <sup>4</sup>UCLouvain, TECLIM - Georges Lemaître Centre for Earth and Climate Research, Louvain-la-Neuve, Belgium

11 <sup>5</sup>EcoAct/ ATOS, 35 rue de miromesnil, 75008, Paris, France

12 <sup>6</sup>School of Atmospheric Science, Sun Yat-sen University, Guangzhou, Guangdong, 510275, China

13

14 *Correspondence to:* Haicheng Zhang ([haicheng.zhang@ulb.be](mailto:haicheng.zhang@ulb.be))

15 **Abstract.** Lateral carbon transport from soils to the ocean through rivers has been acknowledged  
16 as a key component of global carbon cycle, but is still neglected in most global land surface  
17 models (LSMs). Fluvial transport of dissolved organic carbon (DOC) and CO<sub>2</sub> has been  
18 implemented in the ORCHIDEE LSM, while erosion-induced delivery of sediment and  
19 particulate organic carbon (POC) from land to river was implemented in another version of the  
20 model. Based on these two developments, we take the final step towards the full representation  
21 of biospheric carbon transport through the land-river continuum. The newly developed model,  
22 called ORCHIDEE-C<sub>lateral</sub>, simulates the complete lateral transport of water, sediment, POC,  
23 DOC and CO<sub>2</sub> from land to sea through the river network, the deposition of sediment and POC in  
24 the river channel and floodplains, and the decomposition of POC and DOC in transit. We  
25 parameterized and evaluated ORCHIDEE-C<sub>lateral</sub> using observation data in Europe. The model  
26 explains 94%, 75% and 83% of the spatial variations of observed riverine water discharges,  
27 bankfull water flows and riverine sediment discharges in Europe, respectively. The simulated  
28 long-term average total organic carbon concentrations and DOC concentrations in river flows are  
29 comparable to the observations in major European rivers, although our model generally  
30 overestimates the seasonal variation of riverine organic carbon concentrations. Application of  
31 ORCHIDEE-C<sub>lateral</sub> for Europe reveals that the lateral carbon transfer affects land carbon  
32 dynamics in multiple ways and omission of this process in LSMs may lead to an overestimation of  
33 4.5% in the simulated annual net terrestrial carbon uptake over Europe. Overall, this study presents a  
34 useful tool for simulating large scale lateral carbon transfer and for predicting the feedbacks  
35 between lateral carbon transfer and future climate and land use changes.

## 36 **1 Introduction**

37 Lateral transfer of organic carbon along the land-river-ocean continuums, involving both spatial  
38 redistribution of terrestrial organic carbon and the vertical land-atmosphere carbon exchange, has  
39 been acknowledged as a key component of the global carbon cycle (Ciais et al., 2013; Ciais et  
40 al., 2021; Drake et al., 2018; Regnier et al., 2013, [2022](#)). Erosion of soils and the associated  
41 organic carbon, but also leaching of soil dissolved organic carbon (DOC), represent a non-  
42 negligible leak in the terrestrial carbon budget and a substantial source of allochthonous organic  
43 carbon to inland waters and oceans (Battin et al., 2009; Cole et al., 2007; Raymond et al., 2013;  
44 Regnier et al., 2013). As a result of soil aggregate breakdown and desorption, the accelerated  
45 mineralization of these eroded and leached soil carbon loads leads to considerable CO<sub>2</sub> emission  
46 to the atmosphere (Chappell et al., 2016; Lal, 2003; Van Hemelryck et al., 2011). Meanwhile, the  
47 organic carbon that is redeposited and buried in floodplains and lakes might be preserved for a  
48 long time, thus creating a CO<sub>2</sub> sink (Stallard, 1998; Van Oost et al., 2007; Wang et al., 2010;  
49 Hoffmann, 2022). In addition, lateral redistribution of soil material can alter land-atmosphere  
50 CO<sub>2</sub> fluxes indirectly by affecting soil nutrient availability, terrestrial vegetation productivity and  
51 physiochemical properties of inland and coastal waters (Beusen et al., 2005; Vigiak et al., 2017).

52 Although the important role of lateral carbon transfer in the global carbon cycle has been widely  
53 recognized, to date, the estimates of land carbon loss to inland waters, the fate of the terrestrial  
54 organic carbon within inland waters, as well as the net effect of lateral carbon transfer on land-  
55 atmosphere CO<sub>2</sub> fluxes remain largely uncertain (Berhe et al., 2007; Doetterl et al., 2016; Lal,  
56 2003; Stallard, 1998; Wang et al., 2014b; Zhang et al., 2014). Existing estimates of global carbon  
57 loss from soils to inland waters vary from 1.1 to 5.1 Pg (=10<sup>15</sup> g) C per year (yr<sup>-1</sup>) (Cole et al.,  
58 2007; Drake et al., 2018), and the estimated net impact of global lateral carbon redistribution on  
59 land-atmosphere carbon budget ranges from an uptake of atmospheric CO<sub>2</sub> by 1 Pg C yr<sup>-1</sup> to a  
60 land CO<sub>2</sub> emission of 1 Pg C yr<sup>-1</sup> (Lal, 2003; Stallard, 1998; Van Oost et al., 2007; Wang et al.,  
61 2017; [Regnier et al., 2022](#)). A reliable model which is able to explicitly simulate the lateral  
62 carbon flux along the land-river continuum and also the interactions between these lateral fluxes  
63 and the comprehensive terrestrial carbon cycle, would thus be necessary for projecting changes  
64 in the global carbon cycle more accurately.

65 Global land surface models (LSMs) are important tools to simulate the feedbacks between  
66 terrestrial carbon cycle, increasing atmospheric CO<sub>2</sub>, and climate and land use change. However,  
67 the lateral carbon transfer, especially for the particulate organic carbon (POC), is still missing or  
68 incompletely represented in existing LSMs (Lauerwald et al., 2017; Lauerwald et al., 2020;  
69 Lugato et al., 2016; Naipal et al., 2020; Nakhavali et al., 2021; Tian et al., 2015). It has been  
70 hypothesized that the exclusion of lateral carbon transfer in LSMs implies a significant bias in  
71 the simulated global land carbon budget (Ciais et al., 2013; Ciais et al., 2021; Janssens et al.,  
72 2003). For instance, the study of Nakhavali et al. (2021) suggested that about 15% of the global  
73 terrestrial net ecosystem production is exported to inland waters as leached DOC. Lauerwald et  
74 al. (2020) showed that the omission of lateral DOC transfer in LSM might lead to significant  
75 underestimation (8.6%) of the net uptake of atmospheric carbon in the Amazon basin while  
76 terrestrial carbon storage changes in response to the increasing atmospheric CO<sub>2</sub> concentrations  
77 were overestimated.

78 Over the past decade, a number of LSMs have been developed which represent leaching of DOC  
79 from soils (Nakhavali et al. 2018, Kicklighter et al. 2013) or the full transport of DOC through  
80 the land-river continuum (Lauerwald et al., 2017; Tian et al., 2015). However, the erosion-  
81 induced transport of soil POC, which has also been reported to be able to affect the carbon  
82 balance of terrestrial ecosystems strongly (Lal., 2003; Van Oost et al., 2007; Tian et al., 2015), is  
83 still not or poorly represented in LSMs. The explicit simulation of the complete transport process  
84 of POC at large spatial scales is still a major challenge, due to the complexity of the processes  
85 involved, including erosion-induced sediment and POC delivery to rivers, deposition of  
86 sediment and POC in river channels and floodplains, re-detachment of the previously deposited  
87 sediments and POC, decomposition and transformation of POC in riverine and flooding waters,  
88 as well as the changes of soil profile caused by erosion and deposition (Doetterl et al., 2016;  
89 Naipal et al., 2020; Zhang et al., 2020).

90 Several recent model developments have led to the implementation of the lateral transfer of POC  
91 in large-scale LSMs. Despite this, there are still some inevitable limitations in these  
92 implementations. The Dynamic Land Ecosystem Model (DLEM v2.0, Tian et al., 2015) is able  
93 to simulate the erosion-induced POC loss from soil to river and the transport and decomposition  
94 of POC in river networks. However, it does not represent the POC deposition in floodplains, nor

95 the impacts of soil erosion and floodplain deposition on the vertical profiles of soil organic  
96 carbon (SOC). The Carbon Erosion DYNAMics model (CE-DYNAM, Naipal et al., 2020)  
97 simulates erosion of SOC and its re-deposition on the toe-slope or floodplains, transport of POC  
98 along river channels, as well as the impact on SOC dynamics at the eroding and deposition sites.  
99 However, running at annual time scale, it mostly addresses the centennial timescale and does not  
100 represent deposition and decomposition of POC in river channels. Moreover, CE-DYNAM was  
101 only applied over the Rhine catchment and has not been fully coupled into a land surface model,  
102 therefore excluding the feedbacks of soil erosion on the fully coupled land and aquatic carbon  
103 cycles. There are of course more dedicated hydrology and soil erosion models that explicitly  
104 simulate the complete transport, deposition and decomposition processes of POC in small river  
105 basins (e.g. Jetten et al., 2003; Nearing et al., 1989; Neitsch et al., 2011). However, it is difficult  
106 to apply these models at large spatial scales (e.g. continental or global scale) due to the limited  
107 availability of forcing data (e.g. geometric attributes of river channel), suitable model  
108 parameterization and computational capacity. Moreover, these models have limited capability of  
109 representing the full terrestrial C cycle in response to climate change, increasing atmospheric  
110 CO<sub>2</sub> and land use change. Therefore, basin-scale models are not an option to assess the impact of  
111 soil erosion on the large-scale terrestrial C budget in response to global changes.

112 Here we describe the development, application and evaluation of a new branch of the  
113 ORCHIDEE LSM (Krinner et al., 2005), hereafter ORCHIDEE-C<sub>lateral</sub>, that can be used to  
114 simulate the complete lateral transfer processes of water, sediment, POC and DOC along the  
115 land-river-ocean continuum at large spatial scale (e.g. continental and global scale). In previous  
116 studies, the leaching and fluvial transfer of DOC and the erosion-induced delivery of sediment  
117 and POC from upland soil to river network have been implemented in two different branches of  
118 the ORCHIDEE LSM (i.e. ORCHILEAK (Lauerwald et al., 2017) and ORCHIDEE-MUSLE  
119 (Zhang et al., 2020)). For this new branch, we first merged these two branches, and subsequently  
120 implemented the fluvial transfer of sediment and POC in the coupled model. ORCHIDEE-C<sub>lateral</sub>  
121 is calibrated and evaluated using observation data of runoff, bankfull flow, and riverine loads and  
122 concentrations of sediment, POC and DOC across Europe. By applying the calibrated model at  
123 European scale, we estimate the magnitude and spatial distribution of the lateral carbon transfer  
124 in European catchments during the period 1901-2014, as well as the potential impacts of lateral  
125 carbon transfer on the land carbon balance. Comparing simulations results to those of an

126 alternative simulation run with lateral displacement of C deactivated, we finally quantify the  
127 biases in simulated land C budgets that arise ignoring the lateral transfers of C along the land-  
128 river continuum.

129

## 130 **2 Model development and evaluation**

### 131 **2.1 ORCHIDEE land surface model**

132 The ORCHIDEE LSM comprehensively simulates the cycling of energy, water and carbon in  
133 terrestrial ecosystems (Krinner et al., 2005). The hydrological processes (e.g. rainfall  
134 interception, evapotranspiration and soil water dynamics) and plant photosynthesis in  
135 ORCHIDEE are simulated at a time step of 30 minutes. The carbon cycle processes (e.g.  
136 maintenance and growth respiration, carbon allocation, litter decomposition, SOC dynamics,  
137 plant phenology and mortality) are simulated at daily time step. In its default configuration,  
138 ORCHIDEE represents 13 land cover types, with one for bare soil and 12 for lands covered by  
139 vegetation (eight types of forests, two types of grasslands, two types of croplands). Given  
140 appropriate land cover maps and parametrization, the number of PFTs to be represented can  
141 however be adapted (Zhang et al., 2020).

142 Our previous implementations of lateral DOC transfer (Lauerwald et al., 2017) and of POC  
143 delivery from upland to river network (Zhang et al., 2020) were both based on the ORCHIDEE  
144 branch ORCHIDEE-SOM (Camino-Serrano et al., 2018, Fig. S1), which provides a depth-  
145 dependent description of the water and carbon dynamics in soil column. In specific, the vertical  
146 soil profile in ORCHIDEE-SOM is described by an 11-layer discretization of a 2 m soil column  
147 (Camino-Serrano et al., 2018). Water flows between adjacent soil layers are simulated using the  
148 Fokker–Planck equation that resolves water diffusion in non-saturated conditions (Campoy et al.,  
149 2013; Guimberteau et al., 2018). Free gravitational drainage occurs in the lowest soil layer when  
150 actual soil water content is higher than the residual water content (Campoy et al., 2013).

151 Following the CENTURY model (Parton et al., 1988), ORCHIDEE-SOM represents two litter  
152 pools (metabolic and structural) and three SOC pools (active, slow and passive) that differ in  
153 their respective turnover times. The decomposition of each carbon pool is calculated by first  
154 order kinetics based on the corresponding turnover time, soil moisture and temperature as

155 controlling factors, as well as the priming effects of fresh organic matter (Guenet et al., 2018;  
156 Guenet et al., 2016). Soil DOC is represented by a labile and a ~~stable~~refractory DOC pools, with  
157 a high and low turnover rate, respectively. Each DOC pool may be in the soil solution or  
158 adsorbed on the mineral matrix. The products of litter and SOC decomposition enter the free  
159 DOC pool, which in turn is decomposed following first order kinetics (Kalbitz et al., 2003) and  
160 returns back to SOC. Adsorption and desorption of DOC follows an equilibrium distribution  
161 coefficient calculated from soil clay and pH. Free DOC can be transported with the water flux  
162 simulated by the soil hydrological module of ORCHIDEE. However, DOC adsorbed to soil  
163 minerals can neither be decomposed nor transported (Camino-Serrano et al., 2018). All the  
164 described processes occur within each soil layer. At each time step, “the flux of DOC leaving the  
165 soil is calculated by multiplying DOC concentrations in soil solution with the runoff (surface  
166 layer) and drainage (bottom layer) flux simulated by the hydrological module” (Camino-Serrano  
167 et al., 2018, p. 939). More detailed information about the simulation of soil hydrological and  
168 biogeochemical processes in ORCHIDEE-SOM can be found in Guenet et al. (2016) and  
169 Camino-Serrano et al. (2018).

### 170 **2.1.1 Lateral transfer of DOC and CO<sub>2</sub>**

171 Lateral transfer of DOC and dissolved CO<sub>2</sub> from land to ocean through river network has been  
172 implemented in the ORCHILEAK (Lauerwald et al., 2017), an ORCHIDEE branch developed  
173 from ORCHIDEE-SOM (Fig. S1). ~~The~~The method used in ORCHILEAK to simulate the  
174 adsorption, desorption, production, consumption and transport of DOC within the soil column, as  
175 well as DOC export from the soil to river along column with surface runoff and drainage is  
176 similar to that used in ORCHILEAK is simulated using the same method as ORCHIDEE-SOM.  
177 Besides the decomposition of SOC and litter, ORCHILEAK also represents the contribution of  
178 wet and dry deposition to soil DOC via throughfall. The direct DOC input from rainfall to  
179 aquatic DOC pools is simulated based on the DOC concentration in rainfall and the area fraction  
180 of stream and flooding waters in each basin—(Table 1). Note that the maximum area fractions of  
181 river surface and floodplain in each basin (i.e. each 0.5°×0.5° grid cell in this study) are derived  
182 from high-resolution topographic data (Table 1). As it is difficult to explicitly represent all real  
183 river channels in a global land surface model (due to the limit of computing efficiency of current  
184 computers), we assume that there is one virtual river channel in each 0.5°×0.5° pixel. The surface

185 area of this virtual river is the sum of all real rivers and the flow direction of this virtual is  
 186 assumed to be same to the largest real river (Lauerwald et al., 2015).

187 Simulation of the lateral transfer of DOC and CO<sub>2</sub> in river networks, i.e. the transfer of DOC and  
 188 CO<sub>2</sub> from one basin to another based on the stream flow directions obtained from a forcing file  
 189 (0.5°, Table 1), follows the routing scheme of water (Guimberteau et al., 2012). For each basin  
 190 with floodplain (defined by forcing data), bankfull flow occurs when stream volume in the river  
 191 channel exceeds a threshold prescribed by the forcing file (Table 1). DOC and CO<sub>2</sub> in flooding  
 192 waters can enter into soil DOC and CO<sub>2</sub> pools along with the ~~infiltrating water~~ flooding water  
 193 infiltrated into soil. The infiltration rate of flooding water depends on soil properties and soil  
 194 water content, but does not depend on vegetation cover. On the contrary, DOC and CO<sub>2</sub>  
 195 originated from the decomposition of submerged litter and SOC in the floodplains are added to  
 196 the overlying flooding waters. Note that the turnover times of litter and SOC under flooding  
 197 waters are assumed to be three times of the litter and SOC turnover times in upland soil (Reddy  
 198 & Patrick Jr, 1975; Neckles & Neill, 1994; Lauerwald et al., 2017). After removing the  
 199 infiltrated and evaporated water, the amount of the remaining flooding water, as well as the DOC  
 200 and dissolved CO<sub>2</sub> returning to river channel at the end of each day is calculated based on a time  
 201 constant of flooding water (= 4.0 days, d'Orgeval et al., 2008) modified by a basin-specific  
 202 topographic index ( $f_{topo}$ , unitless) (Lauerwald et al., 2017).

203

204 **Table 1.** List of forcing data needed to run ORCHIDEE-C<sub>lateral</sub> and the data used to evaluate the  
 205 simulation results. S<sub>res</sub> and T<sub>res</sub> are the spatial and temporal resolution of the forcing data,  
 206 respectively.

	Data	S <sub>res</sub>	T <sub>res</sub>	Data source
Forcing	Climatic forcing data (precipitation, temperature, incoming shortwave/longwave radiation, air pressure, wind speed, relative humidity)	0.5°	3 hour	GSWP3 database (Dirmeyer et al., 2006)
	Land cover	0.5°	1 year	LUHa.rc2 database (Chini et al., 2014)
	Soil texture class	0.5°	–	Reynolds et al. (1999)



	Soil bulk density and pH	30"	–	HWSD v1.2 (FAO/IIASA/ISRIC/ISSCAS/JRC, 2012)
	Stream flow directions, topographic index ( $f_{topo}$ )	0.5°	–	STN-30p (Vörösmarty et al., 2000)
	Area fraction of floodplains	250 m	–	GFPLAIN250m (Nardi et al., 2019) <sup>a</sup>
	Area fraction of river surface	0.5°	–	Lauerwald et al. (2015)
	Maximum water storage in river channel ( $S_{rivmax}$ )	0.5°	–	Derived from pre-runs with ORCHIDEE-C <sub>lateral</sub> (see section 2.3)
	Reference sediment delivery rate ( $SED_{ref}$ )	0.5°	–	Zhang et al. (2020)
	Digital Elevation Model (DEM)	3"	–	HydroSHEDS (Lehner et al., 2008) and GDEM v3 (Abrams et al., 2020) <sup>b</sup>
	Riverine water discharge	–	1 day	GRDC <sup>c</sup>
	Bankfull flow	–	1 year	Schneider et al. (2011)
	Sediment delivery from upland to inland waters	100 m	1 year	Borrelli et al. (2018)
Validation	Riverine sediment discharge	–	1 year	European Environment Agency <sup>d</sup> and publications <sup>e</sup>
	Riverine POC and DOC concentration	–	Instantaneous	GLORICH (Hartmann et al., 2019)
		30"		HWSD v1.2
		5'		GSDE (Shangguan et al., 2014)
	SOC stock	250 m	–	SoilGrids (Hengl et al., 2014)
		10 km		S2017 (Sanderman et al., 2017)
		250 m		LandGIS <sup>f</sup>

207 <sup>a</sup> The GFPLAIN250m only covers the regions south of 60° N. We produced map of floodplain distribution in  
208 regions north of the 60° N using the same method for producing GFPLAIN250m (Nardi et al., 2019) based on the  
209 ASTER GDEM v3 database (Abrams et al., 2020). <sup>b</sup> The DEM data from HydroSHEDS and GDEM v3 are used to  
210 extract the topographic properties (e.g. location, area and average slope) of headwater basins in regions south and  
211 north of 60° N, respectively. <sup>c</sup> The Global Runoff Data Centre, 56068 Koblenz, Germany. <sup>d</sup>  
212 <https://www.eea.europa.eu/data-and-maps/data/sediment-discharges>. <sup>e</sup> Publications including Van Dijk & Kwaad,  
213 1998; Vollmer & Goelz, (2006) and Reports of the DanubeSediment project (Sediment Management Measures for  
214 the Danube, <http://www.interreg-danube.eu/approved-projects/danubesediment>). <sup>f</sup>  
215 [https://zenodo.org/record/2536040#\\_YC-QGo9KiUm](https://zenodo.org/record/2536040#_YC-QGo9KiUm).

216

217 Decomposition of DOC in stream and flooding waters is calculated at daily time step based on  
 218 the prescribed turnover times of labile (2 days) and refractory (80 days) DOC in waters (when  
 219 temperature is 28 °C) and a temperature factor obtained from Hanson et al. (2011). CO<sub>2</sub> evasion  
 220 in inland waters is simulated using a much ~~fine~~finer integration time step of 6 minutes. The CO<sub>2</sub>  
 221 partial pressures ( $p\text{CO}_2$ ) in water column is first calculated based on the temperature-dependent  
 222 solubility of CO<sub>2</sub> and the concentration of dissolved CO<sub>2</sub> (Telmer and Veizer, 1999). Then the  
 223 CO<sub>2</sub> evasion is calculated based on the gas exchange velocity, the water–air gradient in  $p\text{CO}_2$ ,  
 224 and the surface water area available for gas exchange (Lauerwald et al., 2017). The effect of  
 225 wind speed on CO<sub>2</sub> evasion is not represented in the current version of ORCHILEAK. In  
 226 addition, swamp and wetland are ~~also~~ represented in the routing scheme of ORCHILEAK. More  
 227 detailed descriptions can be found in Lauerwald et al. (2017).

### 228 2.1.2 Sediment and particulate organic carbon delivery from upland soil to river network

229 To give an accurate simulation of sediment delivery from uplands to river network and maintain  
 230 computational efficiency, an upscaling scheme which integrates information from high-resolution (3")  
 231 topographic and soil erodibility data into a LSM forcing file at 0.5° spatial resolution, has been introduced  
 232 (see details in Zhang et al., 2020, Fig. S2\_1). With this upscaling scheme, the erosion-induced sediment  
 233 and POC delivery from upland soils to the river network, as well as the changes in SOC profiles due to  
 234 soil erosion had already been implemented in ORCHIDEE-MUSLE (Zhang et al., 2020). The sediment  
 235 delivery from small headwater basins (which are basins without perennial stream and are extracted from  
 236 high-resolution (e.g. 3") digital elevation model (DEM) data, Figs. S2a1a&d) to the river network (i.e.  
 237 gross upland soil erosion – sediment deposition within headwater basins) is simulated using the Modified  
 238 Universal Soil Loss Equation model (MUSLE, Williams, 1975). As introduced in Zhang et al. (2020),  
 239 “the daily sediment delivery rate from each headwater basin ( $S_{i\_ref}$ , Mg day<sup>-1</sup> basin<sup>-1</sup>) is first calculated for  
 240 a given set of reference runoff and vegetation cover conditions (Fig. S2e1e):

$$241 \quad S_{i\_ref} = a(Q_{i\_ref} q_{i\_ref})^b K_i L S_i C_{ref} P_{ref} \quad (1)$$

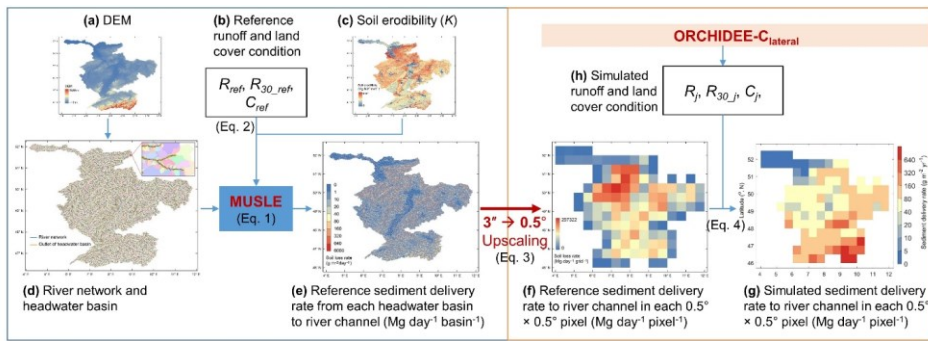
242 where  $Q_{i\_ref}$  is the total water discharge (m<sup>3</sup> day<sup>-1</sup>) at the outlet of headwater basin  $i$  for the daily  
 243 reference runoff condition ( $R_{ref}$ ) of 10 mm day<sup>-1</sup> (see Table S1 for the definitions of all  
 244 abbreviations used in this study). In Eq. 1,  $q_{i\_ref}$  is the daily peak flow rate (m<sup>3</sup> s<sup>-1</sup>) at the  
 245 headwater basin outlet under the assumed reference runoff condition. Similar to the SWAT  
 246 model (Soil and Water Assessment Tool, Neitsch et al., 2011),  $q_{i\_ref}$  was calculated from the

247 reference maximum 30-minutes runoff (= 1 mm 30-minutes<sup>-1</sup>) depth and drainage area ( $DA_i$ , m<sup>2</sup>)  
 248 according to the following equation:

$$249 \quad q_{i,ref} = \frac{R_{30,ref}}{30 \times 60} \left( DA_i^{(d DA_i^c)} \right) 1000 \quad (2)$$

250 where  $R_{30,ref}$  (= 1 mm 30-minutes<sup>-1</sup>) is the assumed daily maximum 30-minutes runoff<sup>3</sup>. The  
 251 coefficients  $a$  and  $b$  in Eq. 1 and  $c$  and  $d$  in Eq. 2 need to be calibrated (see section 2.3 and Table  
 252 2). In Eq. 1, the term  $LS_i$  is the combined dimensionless slope length and steepness factor  
 253 calculated based on the  $DA_i$  and the average slope steepness (extracted from DEM) of headwater  
 254 basin  $i$  (Moore and Wilson, 1992).  $C_{ref}$  (0-1, dimensionless) in Eq. 1 represents the cover  
 255 management factor which depends on vegetation cover and storage of plant debris (see below).  
 256 The value of  $C_{ref}$  is set to 0.1 for the reference state. The soil erodibility factor  $K_i$  (Mg MJ<sup>-1</sup> mm<sup>-1</sup>)  
 257 <sup>1</sup> is calculated using the method of the EPIC model (Sharpley and Williams, 1990) based on  
 258 SOC and soil texture data obtained from the GSDE database (Table 1). The term  $P_{ref}$  (0-1,  
 259 dimensionless) in Eq. 1 is a factor representing erosion control practices. It was set to 1, as we  
 260 did not consider the impacts of soil conservation practices in reducing soil erosion rate. Note that  
 261 it does not matter which value is chosen for the  $R_{ref}$ ,  $R_{30,ref}$  and  $C_{ref}$  as long as they are used  
 262 consistently throughout a study.

Formatted: English (United States)



263 **Figure 1** Upscaling scheme used in ORCHIDEE-MUSLE (Zhang et al., 2020) and ORCHIDEE-  
 264  $C_{lateral}$  for calculating the sediment delivery rate from headwater basins to river networks.  
 265 MUSLE is the Modified Universal Soil Loss Equation; DEM is the digital elevation model (m);  
 266  $K$  is the soil erodibility factor (Mg MJ<sup>-1</sup> mm<sup>-1</sup>);  $R_{ref}$  is the assumed reference daily runoff depth  
 267 (= 10 mm day<sup>-1</sup>);  $R_{30,ref}$  is the assumed reference maximum 30-minutes runoff<sup>3</sup> depth (= 1 mm  
 268 day<sup>-1</sup>).

269 30-minutes<sup>-1</sup>);  $C_{ref}$  (= 0.1, dimensionless) is the assumed reference cover management factor;  
 270  $R_{iday}$ ,  $R_{30\ iday}$  and  $C_{iday}$  are the simulated daily total runoff depth, daily maximum 30-minutes  
 271 runoff depth and daily cover management factor, respectively. This figure is adapted from the  
 272 Fig. 1 in Zhang et al. (2020).

273  
 274 For the use of these reference sediment delivery estimates in ORCHIDEE-C<sub>lateral</sub>, the values were  
 275 first calculated for each headwater basin derived from high resolution geodata (Fig. [S2e1e](#)), then  
 276 aggregated to 0.5° grid cells (Fig. [S2f1f](#)) – the scale used in our simulations and required to  
 277 maintain computational efficiency (also limited by the availability of climate and land cover  
 278 forcing data).

279 This aggregated dataset is then used to force the simulation of the actual daily sediment delivery  
 280 ( $S_j$ , g day<sup>-1</sup> grid<sup>-1</sup>) in ORCHIDEE-C<sub>lateral</sub>, simply based on the estimated reference sediment  
 281 delivery rates of Eq. (1) and on the ratios between actual runoff and land cover conditions and  
 282 the assumed reference conditions used to create that forcing file (Eq. 4, Fig. [S2g1g](#)).

$$283 \quad S_{ref} = \sum_{i=1}^n (S_{i,ref}) \times 10^6 \quad (3)$$

$$284 \quad S_j = S_{ref} \left( \frac{R_j R_{30,j}}{R_{ref} R_{30,ref}} \right)^b \frac{C_j}{C_{ref}} \quad (4)$$

285 where  $R_j$  (mm day<sup>-1</sup>) is the total surface runoff on day  $j$  simulated by the hydrological module or  
 286 ORCHIDEE-MUSLE at 0.5° spatial resolution every 30 minutes.  $R_{30,j}$  (mm 30-min<sup>-1</sup>) is the  
 287 maximum value of the 48 half-hour runoffs in each day.  $C_j$  (0-1, unitless) is the daily actual  
 288 cover management factor, calculated based on the fraction of surface vegetation cover, the  
 289 amount of litter [carbonstock](#) and the biomass of living roots in each PFT within each 0.5°×0.5°  
 290 grid cell.  $R_{ref}$ ,  $R_{30,ref}$ ,  $C_{ref}$  and  $P_{ref}$  are the reference values used to estimate the reference  
 291 sediment delivery rates as describe above.

292 Daily POC delivery to river headstream in each 0.5° grid cell is finally simulated based on the  
 293 sediment delivery rate and the average SOC concentration of surface soil layers (0-20 cm). [We](#)  
 294 [assumed that litter cannot be eroded and transported to the river network, however, it can affect](#)  
 295 [soil erosion rate through the cover management factor of the MUSLE model \(denoted by  \$C\_j\$ , Eq.](#)  
 296 [4\).](#) The vertical SOC profile is updated every day based on the average depth of eroded soil for

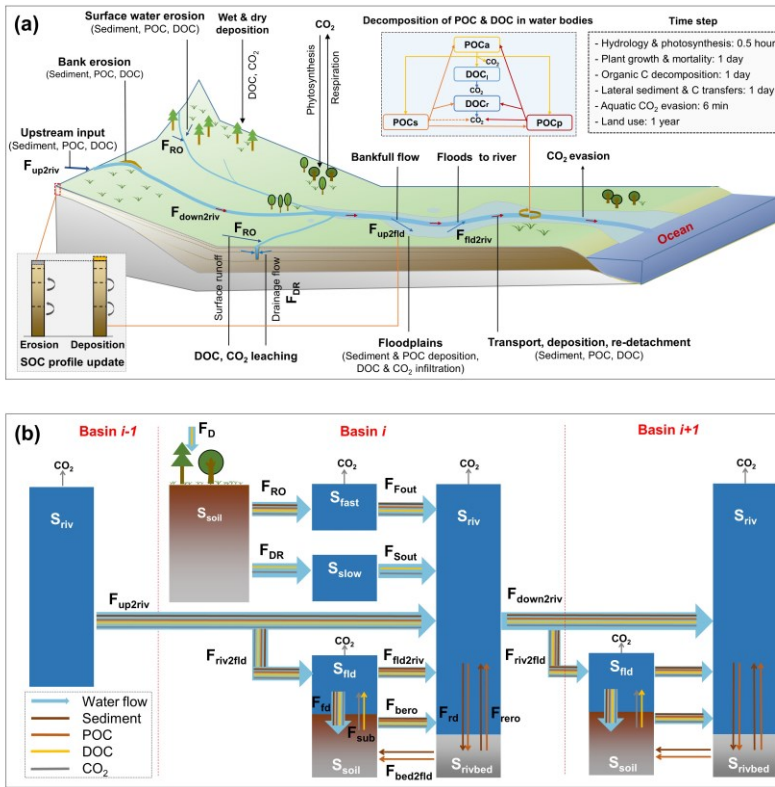
297 each PFT in each 0.5° grid cell of ORCHIDEE. For more detailed description of the  
 298 ORCHIDEE-MUSLE, we refer to Zhang et al. (2020).

299

300 **2.2 Sediment and POC transport in inland water network**

301 Through the merge of the model branches ORCHILEAK and ORCHIDEE-MUSLE, the new  
 302 branch ORCHIDEE-C<sub>lateral</sub> combines the novel features of both sources (DOC and POC)  
 303 described above. The development of ORCHIDEE-C<sub>lateral</sub> is complemented by a representation of  
 304 the sediment and POC transport through the river network that is completely novel and described  
 305 below.

306 **2.2.1 Sediment transport**



307

308 **Figure 42** Simulated lateral transfer processes of water, sediment and carbon (POC, DOC and  
309 CO<sub>2</sub>) in ORCHIDEE-C<sub>lateral</sub> (a) and a schematic plot for the reservoirs and flows of water,  
310 sediment and carbon represented in the routing module of ORCHIDEE-C<sub>lateral</sub> (b). S<sub>soil</sub> is the soil  
311 pool. S<sub>rivbed</sub> is the sediment (also POC) deposited on the river bed. S<sub>fast</sub>, S<sub>slow</sub>, S<sub>riv</sub> and S<sub>fld</sub> are the  
312 ‘fast’, ‘slow’, stream and flooding water reservoir, respectively. F<sub>RO</sub> and F<sub>DR</sub> are the surface  
313 runoff and belowground drainage, respectively. F<sub>Fout</sub> and F<sub>Sout</sub> are the flows from fast and slow  
314 reservoir to the stream reservoir, respectively. F<sub>up2riv</sub> and F<sub>down2riv</sub> are the upstream inputs and  
315 downstream outputs, respectively. F<sub>riv2fld</sub> is the outputs from river stream to the flooding  
316 reservoir. F<sub>fld2riv</sub> is the return flow from flooding reservoir to stream reservoir. F<sub>bed2fld</sub> is the  
317 transform from deposited sediment in river bed to floodplain soil. F<sub>bero</sub> is bank erosion. F<sub>rd</sub> and  
318 F<sub>ero</sub> are the deposition and re-detachment of sediment and POC in river channel, respectively.  
319 F<sub>sub</sub> is the flux of DOC and CO<sub>2</sub> from floodplain soil (originated from the decomposition of  
320 submerged litter and soil carbon) to the overlying flooding water. F<sub>fd</sub> is the deposition of  
321 sediment and POC and the infiltration of water and DOC. F<sub>D</sub> is the wet and dry deposition of  
322 DOC from atmosphere and plant canopy. DOC<sub>l</sub> and DOC<sub>r</sub> are the labile and refractory DOC  
323 pool, respectively. POC<sub>a</sub>, POC<sub>s</sub> and POC<sub>p</sub> are the active, slow and passive POC pool,  
324 respectively.

325 Simulation of sediment transport through the river network basically follows the routing scheme  
326 of surface water and DOC of ORCHILEAK (Fig. 42). Along with surface runoff ( $F_{RO\_h2o}$ , m<sup>3</sup>  
327 day<sup>-1</sup>), the sediment delivery ( $F_{RO\_sed}$ , g day<sup>-1</sup>) from uplands in each basin (i.e. each 0.5° grid cell  
328 in the case of this study) initially feeds an aboveground water reservoir ( $S_{fast\_h2o}$ , m<sup>3</sup>) with a so-  
329 called fast water residence time. From this fast water reservoir, a delayed outflow feeds into the  
330 so-called stream reservoir ( $S_{riv}$ , m<sup>3</sup>, Fig. 42b). Daily water ( $F_{Fout\_h2o}$ , m<sup>3</sup> day<sup>-1</sup>) and sediment  
331 ( $F_{Fout\_sed}$ , g day<sup>-1</sup>) flows from fast water reservoir to stream reservoir are calculated from a grid  
332 cell-specific topographic index  $f_{topo}$  (unitless, Vörösmarty et al., 2000) extracted from a forcing  
333 file (Table 1) and a reservoir-specific factor  $\tau$  which translates  $f_{topo}$  into a water residence time of  
334 each reservoir (Eqs. 5, 6). Following Guimberteau et al. (2012), the  $\tau$  of the fast water reservoir  
335 ( $\tau_{fast}$ ) is set to 3.0 days. As the sediment delivery calculated from MUSLE is the net soil loss  
336 from headwater basins (gross soil erosion – soil deposition within headwater basins), we  
337 assumed that there is no sediment deposition in the fast reservoir, and that all of the sediment in  
338 the fast reservoir enters the stream reservoir. In addition, only the surface runoff causes soil

339 erosion. The belowground drainage ( $F_{DR\_h2o}$ ,  $m^3 \text{ day}^{-1}$ ) only transports DOC and dissolved  $CO_2$   
 340 to the stream reservoir (Fig. [4b2b](#)).

$$341 \quad F_{Fout\_h2o} = \frac{S_{fast\_h2o}}{\tau_{fast} f_{topo}} \quad (5)$$

$$342 \quad F_{Fout\_sed} = \frac{S_{fast\_sed}}{\tau_{fast} f_{topo}} \quad (6)$$

343 The budget of the suspended sediment in the stream ( $S_{riv\_sed}$ , g) is determined by  $F_{out\_sed}$ , the  
 344 upstream sediment input ( $F_{up2riv\_sed}$ ,  $g \text{ day}^{-1}$ ), the sediment input by flooding water returning to  
 345 the river ( $F_{fld2riv\_sed}$ ,  $g \text{ day}^{-1}$ ), the re-detachment of the previously deposited sediment in the river  
 346 bed ( $F_{rero\_sed}$ ,  $g \text{ day}^{-1}$ ), the bank erosion ( $F_{bero\_sed}$ ,  $g \text{ day}^{-1}$ ), the sediment deposition in the river  
 347 bed ( $F_{rd\_sed}$ ,  $g \text{ day}^{-1}$ ) and the sediment transported to downstream river stretches ( $F_{down2riv\_sed}$ ,  $g$   
 348  $\text{day}^{-1}$ ) and, occasionally, floodplains ( $F_{riv2fld\_sed}$ ,  $g \text{ day}^{-1}$ ) (Eq. 7).

$$349 \quad \frac{dS_{riv\_sed}}{dt} = F_{Fout\_sed} + F_{up2riv\_sed} + F_{fld2riv\_sed} + F_{rero\_sed} + F_{bero\_sed} - F_{rd\_sed} - F_{down2riv\_sed} - F_{riv2fld\_sed} \quad (7)$$

350 Sediment transport capacity ( $TC$ ,  $g \text{ m}^{-3}$ ) is defined as the maximum load concentration of  
 351 suspended sediment that a given flow rate can carry, determines TC and the flow rate determine  
 352 the amount of suspended sediment that can be transported to the downstream grid cell (e.g.  
 353  $F_{down2riv\_sed}$ ,  $F_{riv2fld\_sed}$ ), as well as the amount of suspended. Suspended sediment loads that are  
 354 in excess to maximum possible amount of transported sediment will deposit on the river bed  
 355 ( $F_{rd\_sed}$ ) or the. If sediment loads are below that maximum possible amount, erosion rate of the  
 356 river bed ( $F_{rero\_sed}$ ) or river bank ( $F_{bero\_sed}$ ) takes place (Arnold et al., 1995; Nearing et al., 1989;  
 357 Neitsch et al., 2011).

358 In this study, we used an empirical equation adapted from the WBMsed model, which has been  
 359 proven effective in simulating the suspended sediment discharges in global large rivers (Cohen et  
 360 al., 2014), to estimate the  $TC$  ( $g \text{ m}^{-3}$ ) of suspended sediment concentration in stream flow: ( $g \text{ m}^{-3}$ ):  
 361 3:

$$362 \quad TC = \frac{\omega q_{ave}^{0.3} A^{0.5} \left(\frac{q_{iday}}{q_{ave}}\right)^{e_1} (24 \times 60 \times 60)}{F_{down2riv\_h2o}} \quad (8)$$

$$363 \quad e_1 = 1.5 - \max(0.8, 0.145 \log_{10} DA) \quad (9)$$

Formatted: Font: Not Italic

Formatted: Not Superscript/ Subscript

Formatted: Font: Not Italic, Not Superscript/ Subscript

364 where  $\omega$  is the coefficient of proportionality,  $q_{ave}$  ( $\text{m}^3 \text{s}^{-1}$ ) is long-term average stream flow rate  
 365 obtained from an historical simulation by ORCHILEAK (Table 1),  $q_j$  ( $\text{m}^3 \text{s}^{-1}$ ) is stream flow rate  
 366 on day  $j$ ,  $e_l$  is an exponent depending on the upstream drainage area ( $DA$ ,  $\text{m}^2$ ),  $F_{down2riv\_h20}$  ( $\text{m}^3$   
 367  $\text{day}^{-1}$ ) is the daily downstream water discharge from the stream reservoir. In the stream reservoir  
 368 of each basin, net deposition occurs when  $TC$  is smaller than the concentration of suspended  
 369 sediment, and the daily deposited sediment ( $F_{rd\_sed}$ ,  $\text{g day}^{-1}$ ) is calculated based on the surplus of  
 370 the suspended sediment:

$$371 \quad F_{rd\_sed} = c_{rivdep}(S_{riv\_sed} - TC S_{riv\_h20}) \quad (10)$$

372 where  $c_{rivdep}$  (0-1, unitless) is the daily deposited fraction of the sediment surplus. Net erosion of  
 373 the previously deposited sediment in river bed ( $S_{rivbed\_sed}$ , Fig. 42) or the river bank occurs when  
 374  $TC$  is larger than the concentration of suspended sediment. We assumed that the erosion of river  
 375 bank occurs only after all of the  $S_{rivbed\_sed}$  has been eroded. Thus the daily erosion rate ( $F_{rero\_sed}$ ,  $\text{g}$   
 376  $\text{day}^{-1}$ ) in river channel is calculated as:

$$377 \quad F_{rero\_sed} = \begin{cases} c_{ebed}(TC S_{riv\_h20} - S_{riv\_sed}), & c_{ebed}(TC S_{riv\_h20} - S_{riv\_sed}) \leq S_{rivbed\_sed} \\ S_{rivbed\_sed} + c_{ebank}(TC S_{riv\_h20} - S_{riv\_sed} - S_{rivbed\_sed}), & c_{ebed}(TC S_{riv\_h20} - S_{riv\_sed}) > S_{rivbed\_sed} \end{cases} \quad (11)$$

378 where  $c_{ebed}$  (0-1, unitless) and  $c_{ebank}$  (0-1, unitless) are the fraction of sediment deficit that can be  
 379 complemented by erosion of river bed and bank, respectively. After updating the  $S_{riv\_sed}$  based on  
 380 the  $F_{rd\_sed}$  or  $F_{rero\_sed}$ , the sediment discharge to downstream basin ( $F_{down2riv\_sed}$ ,  $\text{g day}^{-1}$ ) is  
 381 calculated based on the ratio of downstream water discharge to the total stream reservoir:

$$382 \quad F_{down2riv\_sed} = (S_{riv\_sed} - F_{rd\_sed} + F_{rero\_sed}) \frac{F_{down2riv\_h20}}{S_{riv\_sh20}} \quad (12)$$

383 In each basin, the bankfull flow occurs when  $S_{riv\_h20}$  exceeds the maximum water storage of river  
 384 channel ( $S_{rivmax}$ ,  $\text{g}$ ), which is defined by a forcing file (Table 1). Sediment flow from stream to  
 385 floodplain ( $F_{riv2fld\_sed}$ ,  $\text{g day}^{-1}$ ) follows the flooding water, and it is calculated as:

$$386 \quad F_{riv2fld\_sed} = (S_{riv\_sed} - F_{rd\_sed} + F_{rero\_sed}) \frac{F_{riv2fld\_h20}}{S_{riv\_sh20}} \quad (13)$$

$$387 \quad F_{riv2fld\_h20} = (S_{riv\_h20} - F_{down2riv\_h20} - S_{rivmax}) \frac{f_{A\_fld}}{f_{A\_fld} + f_{A\_riv}} \quad (14)$$



388 where  $f_{A\_fld}$  (0-1, unitless) and  $f_{A\_riv}$  (0-1, unitless) is the fraction of floodplain area and river  
 389 surface area in each basin, respectively. Following the routing scheme of ORCHILEAK, the  
 390 bankfull flow of a specific basin is assumed to enter the floodplain in the neighbouring  
 391 downstream basin instead of the basin where it originates.

392 The sediment balance in flooding reservoir ( $S_{fld\_sed}$ , g) is controlled by sediment input from the  
 393 upstream basins ( $F_{riv2fld\_sed}$ , g day<sup>-1</sup>), the sediment flowing back to the stream reservoir ( $F_{fld2riv\_sed}$ ,  
 394 g day<sup>-1</sup>) and the sediment deposition ( $F_{fd\_sed}$ , g day<sup>-1</sup>) (Fig. 42):

$$395 \quad \frac{dS_{fld\_sed}}{dt} = F_{riv2fld\_sed} - F_{fld2riv\_sed} - F_{fd\_sed} \quad (15)$$

396 Sediment deposition in floodplain is calculated as the sum of a natural deposition and the  
 397 deposition due to evaporation ( $E_{h2o}$ , m<sup>3</sup> day<sup>-1</sup>) and infiltration ( $I_{h2o}$ , m<sup>3</sup> day<sup>-1</sup>) of the flooding  
 398 waters:

$$399 \quad F_{fd\_sed} = c_{flddep} S_{fld\_sed} + S_{fld\_sed} \frac{E_{h2o} + I_{h2o}}{S_{fld\_h2o}} \quad (16)$$

400 where  $c_{flddep}$  (0-1, unitless) is the daily deposited fraction of the suspended sediment in flooding  
 401 waters. After removing the deposited sediment from  $S_{fld\_sed}$ ,  $F_{fld2riv\_sed}$  is calculated based on the  
 402 ratio of ratio of  $F_{fld2riv\_h2o}$  to the total flooding reservoir:

$$403 \quad F_{fld2riv\_sed} = S_{fld\_sed} \frac{F_{fld2riv\_h2o}}{S_{fld\_h2o} - E_{h2o} - I_{h2o}} \quad (17)$$

404

$$405 \quad F_{fld2riv\_h2o} = \frac{S_{fld\_h2o} - E_{h2o} - I_{h2o}}{\tau_{flood} f_{topo}} \quad (18)$$

406 where  $\tau_{flood}$  is a factor which translates  $f_{topo}$  (Table 1) into a water residence time of the flooding  
 407 reservoir. Same to ORCHILEAK, it is set to 1.4 (day m<sup>-2</sup>) in this study.

408 Note that as the upland soil in ORCHIDEE is composed of clay, silt and sand particles, so that  
 409 the dynamics of clay-, silt- and sand-sediment in inland waters are simulated separately. To  
 410 represent the selective transport of clay-, silt- and sand-sediment, the model parameter  $\omega$  (Eq. 8)  
 411 and  $c_{rivdep}$  (Eq. 10) are set to different values when calculating the sediment transport capacity  
 412 and the deposition of surplus suspended sediment for different particle sizes (Table 2).

413 Moreover, as our model mainly aims to simulate the lateral transfer of sediment and carbon at  
 414 the decadal to centennial timescale, rather than covering the past thousands of years or even  
 415 longer time periods, we did not consider the evolution and diversion of river channels in our  
 416 study.

### 417 2.2.2 POC transport and decomposition

418 Many studies described the selective transport of POC and sediment of different particle sizes.  
 419 The enrichment ratio (defined as the ratios of fraction of any given component in the transported  
 420 sediment to that in the eroded soils) of POC in the transported sediment generally showed  
 421 significant positive correlation to the fine sediment particles (e.g. fine silt and clay), but negative  
 422 correlation to the coarse sediment particles (Galy et al., 2008; Haregeweyn et al., 2008; Nadeu et  
 423 al., 2011; Nie et al., 2015). In ORCHIDEE-C<sub>lateral</sub>, the physical movements of POC in inland  
 424 water systems are simply assumed to follow the flows of finest clay-sediment (Fig. 4b2b). For  
 425 example, the fractions of riverine suspended POC which is deposited on the river bed ( $F_{rd\_POC}$ , g  
 426 C day<sup>-1</sup>) or is transported to the river channel ( $F_{down2riv\_POC}$ , g C day<sup>-1</sup>) or floodplain ( $F_{riv2fld\_POC}$ ,  
 427 g C day<sup>-1</sup>) are assumed to be equal to the corresponding fractions of clay-sediment (Eqs. 19-21).  
 428 Also flows of suspended POC in flooding waters to floodplain soil ( $F_{fd\_POC}$ , g C day<sup>-1</sup>) or back to  
 429 the stream reservoir ( $F_{fld2riv\_POC}$ , g C day<sup>-1</sup>), as well as the resuspension of POC from the river  
 430 bed ( $F_{rero\_POC}$ , g C day<sup>-1</sup>) are scaled to the simulated flows of clay-sediment (Eqs. 22-24). Note  
 431 that, similar to SOC, the POC in aquatic reservoirs are divided into three pools: the active  
 432 ( $POC_a$ ), slow ( $POC_s$ ) and passive pool ( $POC_p$ ) (Fig. 4a2a). The eroded active, slow and passive  
 433 SOC flow into the corresponding POC pools in the ‘fast’ water reservoir (Fig. 4b2b).

$$434 \quad F_{rd\_POC} = S_{riv\_POC} \frac{F_{rd\_sed\_clay}}{S_{riv\_sed\_clay}} \quad (19)$$

$$435 \quad F_{down2riv\_POC} = S_{riv\_POC} \frac{F_{down2riv\_sed\_clay}}{S_{riv\_sed\_clay}} \quad (20)$$

$$436 \quad F_{riv2fld\_POC} = S_{riv\_POC} \frac{F_{riv2fld\_sed\_clay}}{S_{riv\_sed\_clay}} \quad (21)$$

$$437 \quad F_{fd\_POC} = S_{fld\_POC} \frac{F_{fd\_sed\_clay}}{S_{fld\_sed\_clay}} \quad (22)$$

$$438 \quad F_{fld2riv\_POC} = S_{fld\_POC} \frac{F_{fld2riv\_sed\_clay}}{S_{fld\_sed\_clay}} \quad (23)$$

439 
$$F_{bed2fld\_POC} = S_{rivbed\_POC} \frac{F_{bed2fld\_sed}}{S_{rivbed\_sed}} \quad (24)$$

440 The representation of POC dynamics deposition and transformation in the aquatic reservoirs and  
 441 bed sediment involve as well decomposition, which follows largely the scheme used for SOC  
 442 (Fig. 4a2a). However, instead of using the rate modifiers for soil temperature and moisture used  
 443 in the soil carbon module, daily decomposition rates ( $F_{POC\_i}$ , g C day<sup>-1</sup>) of each POC pool  
 444 ( $S_{POC\_i}$ , g C) are simulated to vary with water temperature based on the Arrhenius term which is  
 445 used to simulate the DOC decomposition in ORCHILEAK (Hanson et al., 2011; Lauerwald et  
 446 al., 2017):

447 
$$F_{POC\_i} = S_{POC\_i} \frac{1.073^{(T_{water}-28.0)}}{\tau_{poc\_i}} \quad (25)$$

448 where  $T_{water}$  (°C) is the temperature of water reservoirs and is calculated from local soil  
 449 temperature using an empirical function (Lauerwald et al., 2017). For the POC stored in bed  
 450 sediment, temperature of the stream reservoir is used to calculate the decomposition rate.  $\tau_{POC\_i}$  is  
 451 the turnover time of the  $i$  (active, slow and passive) POC pool. We assumed that the base  
 452 turnover times of active (0.3 year) and slow (1.12 years) POC pools are the same as for the  
 453 corresponding SOC pools. The passive SOC pool is generally regarded as the SOC which is  
 454 associated to soil minerals or enclosed in soil aggregates (Parton et al., 1987). During the soil  
 455 erosion and sediment transport processes, the aggregates break down and the passive POC loses  
 456 its physical protection from decomposition (Chaplot et al., 2005; Hu and Kuhn, 2016; Polyakov  
 457 and Lal, 2008; Wang et al., 2014a). To represent the acceleration of passive POC decomposition  
 458 due to aggregate breakdown, we assume that the turnover time of the passive POC is same to the  
 459 active POC (0.3 year), rather than the passive SOC (462 years). Similar to the scheme used to  
 460 simulate SOC decomposition in ORCHILEAK, the decomposed POC from each of the active,  
 461 slow and passive pool flows to other POC pools, to DOC pools or is released to the atmosphere  
 462 as CO<sub>2</sub> (Fig. 42). Fractions of the decomposed POC flowing to different POC and DOC pools or  
 463 to the atmosphere are set to the same values used in ORCHILEAK for simulating the fates of the  
 464 decomposed SOC pools.

465 Changes in the vertical SOC profile of floodplain soils following sediment deposition is  
 466 simulated at the end of every daily modelling time-step, after physical transfers and

Formatted: Font: 12 pt

467 decomposition of POC have been calculated. The sediment deposited on the floodplain becomes  
468 part of the surface soil layer, and the active, slow and passive POC flow into the active, slow and  
469 passive SOC pools in surface soil layer, respectively. SOC in the original surface and subsurface  
470 soil layers is transferred sequentially to the adjacent deeper soil layers. As the vertical soil profile  
471 in ORCHILEAK is described by an 11-layer discretization of a 2 m soil column, we introduce a  
472 deep (> 2 m) soil pool ( $S_{deep}$ ) to represent the soil and carbon transferred down from the 11<sup>th</sup> soil  
473 layer following ongoing floodplain deposition. Decomposition rates of the organic carbon in this  
474 deep soil pool are assumed to be same to those in the 11<sup>th</sup> (deepest) soil layer. Note that when  
475 the soil erosion rate of the floodplain soil is larger than the sediment deposition rate, sediment  
476 and organic carbon in  $S_{deep}$  move up to replenish the stocks of the 11<sup>th</sup> soil layer.

### 477 2.3 Model application and evaluation

478 In this study, ORCHIDEE-C<sub>lateral</sub> was applied over Europe and parts of Middle East (-30W– 70E,  
479 34N-75N, Fig. S4), where extensive observation datasets are available to calibrate and evaluate  
480 our model (Table 1). The return period of daily bankfull flow ( $P_{flooding}$ , year), which represents  
481 the average interval between two flooding events and is used in this study to produce the forcing  
482 file of  $S_{rivmax}$  from a pre-run of ORCHILEAK. Note that  $P_{flooding}$  is generally shorter than the  
483 return period of real flooding events, as the flooding may occur in several continuous days and  
484 all the flooding waters occurring on these continuous days are generally regarded to belong to  
485 the same flooding event (supplementary Fig. S3S2). To our knowledge, existing observational  
486 data on  $P_{flooding}$  are still very limited. Therefore, following Schneider *et al.* (2011), we also use a  
487 constant  $P_{flooding}$  to simulate the bankfull flows from European rivers and the observed long-term  
488 (1961–2000) average bank full flow rate ( $m^3 s^{-1}$ ) at 66 sites obtained from Schneider *et al.* (2011)  
489 was used to calibrate  $P_{flooding}$  (the optimized value is 0.1 year, Table 2). Following To our  
490 knowledge, there is still no large-scale observation data on the sediment delivery rates from land  
491 to river networks in Europe to our knowledge. Therefore, following Zhang *et al.* (2020), the  
492 parameters a, b, c and d in Eq. 1 and 2 (Table 2) were calibrated at for 57 European catchments  
493 (Fig. S4dS3d) against the modelled sediment delivery data obtained from the European Soil Data  
494 Centre (ESDAC, Borrelli *et al.*, 2018). The sediment delivery data from the ESDAC product is  
495 simulated by the the was derived from WaTEM/SEDEM model simulations using high-resolution  
496 data of topography, soil erodibility, land cover and rainfall. It has been been This model was

Formatted: English (United States)

Formatted: Font: Not Italic, English (United States)

Formatted: English (United States)

Formatted: Font: Not Italic, English (United States)

Formatted: English (United States)

Formatted: Font: Not Italic, English (United States)

Formatted: English (United States)

Formatted: Font: Not Italic, English (United States)

Formatted: English (United States)

Formatted: English (United States)

Formatted: English (United States)

Formatted: English (United States)

Formatted: English (United States)

Formatted: English (United States)

Formatted: English (United States)

497 calibrated and validated using observed sediment fluxes from 24 European catchments (Borrelli  
 498 et al., 2018).

499 Parameters controlling sediment transport, deposition and re-detachment (i.e.  $\omega$ ,  $C_{rivdep}$ ,  $C_{flddep}$ ,  
 500  $C_{ebed}$  and  $C_{ebank}$ , Table 2) in stream and flooding reservoirs were calibrated against the observed  
 501 long-term averaged sediment discharge rate (Table 1). We also conducted a sensitivity analysis  
 502 to test the sensitivity of the simulated riverine sediment and carbon discharges to these  
 503 parameters, following the method used in Tian et al. (2015). The sensitivity of simulation results  
 504 was evaluated based on the relative changes in simulated riverine sediment and carbon  
 505 discharges to a 10% increase and decrease of each parameter (Table 2). Result of the sensitivity  
 506 analysis shows that the simulated riverine sediment and POC discharges are most sensitive to  
 507  $C_{rivdep}$  in Eq. 10, followed by  $\omega$  in Eq. 8 (Fig. SSS4). Compared to  $C_{rivdep}$  and  $\omega$ , the simulated  
 508 riverine sediment and POC discharges are less sensitive to  $C_{flddep}$ ,  $C_{ebed}$  and  $C_{ebank}$ . With 10%  
 509 changes in  $C_{flddep}$ ,  $C_{ebed}$  or  $C_{ebank}$ , the changes in riverine sediment and POC discharges are  
 510 generally less than 3%. In addition, the changes in simulated riverine DOC and CO<sub>2</sub> discharges  
 511 are mostly less than 1% with 10% changes in  $\omega$ ,  $C_{flddep}$ ,  $C_{ebed}$  and  $C_{ebank}$ . Nonetheless, a 10%  
 512 change in  $C_{rivdep}$  can lead to a change of about 5% in the simulated riverine CO<sub>2</sub> discharge (Fig.  
 513 SSS4).

514 **Table 2** Values of the key parameters used in the ORCHIDEE-C<sub>lateral</sub> to simulate the lateral  
 515 transfer of sediment and carbon.

Parameter	Value	Unit	Description	Source
$a$	26.96	Unitless	Coefficient in Eq. 1	Calibrated
$b$	0.76	Unitless	Coefficient in Eq. 1	Calibrated
$c$	1.79	Unitless	Coefficient in Eq. 2	Calibrated
$d$	-0.065	Unitless	Coefficient in Eq. 2	Calibrated
$C_{ebed}$	0.5	Unitless (0-1)	The fraction of sediment deficit that can be complemented by erosion of river bed (Eq. 6)	Calibrated
$C_{ebank}$	0.5	Unitless (0-1)	The fraction of sediment deficit that can be complemented by erosion of river bank (Eq. 6)	Calibrated
$C_{rivdep}$	0.1, 0.2, 0.5 <sup>a</sup>	Unitless (0-1)	Daily deposited fraction of the sediment surplus in stream reservoir (Eq. 5)	Calibrated

Formatted: Font color: Auto, English (United States)

Formatted: English (United States)

$c_{fdep}$	0.5, 1.0, 1.0 <sup>a</sup>	Unitless (0-1)	Daily deposited fraction of the sediment surplus in flooding reservoir (Eq. 11)	Calibrated
$P_{flooding}$	0.1	year	Return period of daily bankfull flow	Calibrated
$\tau_{fast}$	3.0	day	A factor which translates the topographic index into the water residence time of the 'fast' reservoir (Eqs. 5, 6)	Guimberteau et al., 2012
$\tau_{flood}$	1.4	day	A factor which translates the topographic index into the water residence time of the flooding reservoir (Eq. 18)	Guimberteau et al., 2012
$\tau_{poc}$	0.3, 1.12, 0.3 <sup>b</sup>	year	A factor which translates the topographic index into the water residence time of the flooding reservoir (Eq. 25)	Lauerwald et al., 2017
$\omega$	12.0, 5.0, 2.5 <sup>a</sup>	$\text{g s}^{-1}$	Coefficient of proportionality for calculating sediment transport capacity (Eq. 8)	Calibrated

516 <sup>a</sup> For clay, silt and sand sediment, respectively. <sup>b</sup> For active, slow and passive POC, respectively.

517

518 After parameter calibration, ORCHIDEE-C<sub>lateral</sub> was applied to simulate the lateral transfers of  
519 water, sediment and organic carbon in European rivers over the period 1901-2014. Before this  
520 historical simulation, ORCHIDEE-C<sub>lateral</sub> was run over 10,000 years (spin-up) until the soil  
521 carbon pools reached a steady state. In the 'spin-up' simulation, the PFT maps, atmospheric CO<sub>2</sub>  
522 concentrations and meteorological data during 1901–1910 were used repeatedly as forcing data.  
523 The finally simulated water discharge rates in European rivers were evaluated using observation  
524 data at 93 gauging sites (locations see Fig. S4aS3a) from the Global Runoff Data Base (GRDC,  
525 Table 1). The simulated bankfull flows were evaluated against observed long-term (1961–2000)  
526 average bankfull flows at 66 sites (Fig. S4bS3b) from Schneider *et al.* (2011). The simulated  
527 riverine sediment discharge rate is evaluated using observation data from the European  
528 Environment Agency and existing publications (see Table 1) at 221 gauging sites (Fig. S4eS3c).  
529 The riverine total organic carbon (TOC), POC and DOC concentrations provided by the GLOBAL  
530 RIVER Chemistry Database (GLORICH, Hartmann et al., 2019) at 346 sites (Fig. S4dS3d) were  
531 used to evaluate the simulated riverine POC and DOC concentrations. Note that observations in  
532 the GLORICH database which are measured at gauging sites with drainage area  $<1.0 \times 10^4 \text{ km}^2$   
533 were excluded from our model evaluation, because these small catchments cannot be represented  
534 by the coarse river network scheme at 0.5 degree (ca. 55 km at the equator). Among the retained  
535 346 gauging sites, TOC concentrations were measured at 188 sites, DOC was measured at 314

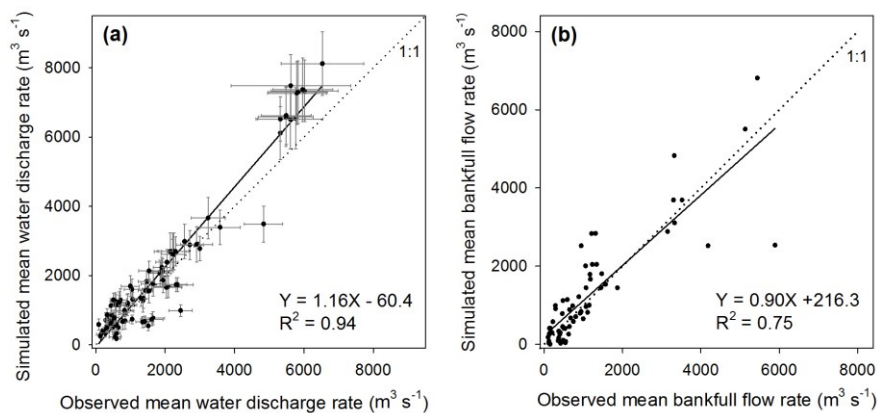
536 sites. POC was measured at only two sites (Bad honnef (51 measurements) and Bimmen (78  
537 measurements)) in the Rhine catchment and one site (Rheine, 36 measurements) in the Ems  
538 catchment (Fig. [S4aS3d](#)).

### 539 **3 Results and Discussion**

#### 540 **3.1 Model evaluation**

##### 541 **3.1.1 Stream water discharge and bankfull flow**

542 Evaluation of our simulation results using *in situ* observation data from Europe rivers indicates  
543 that ORCHIDEE-C<sub>lateral</sub> well reproduces the magnitude and interannual variation of water  
544 discharge rates in major European rivers (Figs. [2a3a](#) and [S6S5](#)). Overall, the simulated riverine  
545 water discharge rate explained 94% (Fig. [2a3a](#)) of the spatial variation of the observed long-term  
546 average water discharge rates across 93 gauging sites in Europe (Fig. [S4aS3a](#)). Relative biases  
547 (calculated as:  $\frac{\text{simulation} - \text{observation}}{\text{observation}} \times 100\%$ , as used through the manuscript if not otherwise  
548 stated) of the simulated average water discharge rates compared to the observations are mostly  
549 smaller than 30% (Fig. [2a3a](#)). For major European rivers, such as the Rhine, Danube, Elbe,  
550 Rhone and Volga, ORCHIDEE-C<sub>lateral</sub> also captures the interannual variation of the water  
551 discharge rate (Fig. [S6S5](#)). We recognize that ORCHIDEE-C<sub>lateral</sub> may overestimate or  
552 underestimate the water discharge rate in some rivers (Fig. [2a3a](#)), particularly in smaller rivers  
553 where discrepancy between the stream routing scheme (delineation of catchment boundaries)  
554 extracted from the forcing data at 0.5° resolution and the real river network (Fig. [S7S6](#)) can be  
555 substantial. An over-estimation or underestimation of the catchment area by the forcing data as  
556 respectively found for the Elbe and Rhine will introduce a proportional bias in the average  
557 amount of simulated discharge from these ~~catchment~~catchments. Another problem are stream  
558 channel bifurcations which occur in reality, but which are not represented in a stream network  
559 derived from a digital elevation model. For example, in the Danube river delta, a fraction of the  
560 discharge is actually exported to the sea through the Saint George Branch, in addition to the  
561 water discharge through the main river channel (Fig. [S7bS6b](#)). This explains why the simulated  
562 water discharge rate at the outlet of the Danube catchment is larger than the observation at the  
563 Ceatal gauging station, Romania (identify number in the GRDC database is 6742900, Fig.  
564 [S6mS5m](#)), where only the main stream discharge was measured.



565

566 **Figure 23** Comparison between observed and simulated riverine water discharge rates (a) and  
 567 bankfull flow rates (b). In figure (a), the error bar denotes the standard deviation of interannual  
 568 variation. Sources of the observed riverine water discharge rate and bankfull flow rate can be  
 569 found in Table 1.

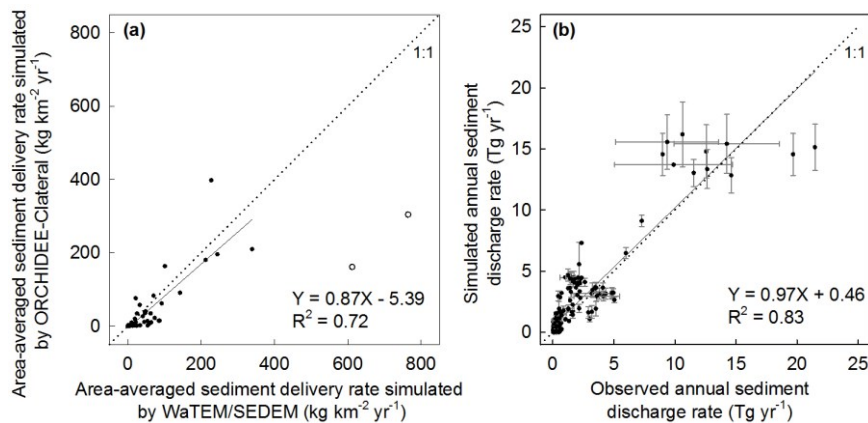
570 With the calibrated return period ( $= 0.1$  year) of the daily flooding rate (see section 2.3), the  
 571 simulated bankfull flow rates compare well to observations at the 66 sites for which data was  
 572 available (Fig. 2b3b). Overall, the simulation result explained 75% of the inter-site variation of  
 573 the observed bankfull flow rates. Relative biases of the simulated bankfull flow rates are  
 574 generally lower than 30%, although the relative bias may be larger than 100% at some sites.

### 575 3.1.2 Sediment transport

576 The simulated area-averaged sediment delivery rates from upland to river network by the  
 577 ORCHIDEE- $C_{lateral}$  are overall comparable to those simulated by the WaTEM/SEDEM for most  
 578 catchments in Europe (Figs. 3a4a and S4dS3d). In the two catchments in the Apennine  
 579 Peninsula, ORCHIDEE- $C_{lateral}$  gives a drastically lower estimation on the sediment delivery rates  
 580 compared to WaTEM/SEDEM. By excluding these two catchments, ORCHIDEE- $C_{lateral}$   
 581 reproduces 72% of the spatial variation of the sediment delivery rates estimated by the  
 582 WaTEM/SEDEM (Fig. 3a4a). In addition, the average sediment loss rate over all catchments  
 583 showed in Fig. S4dS3d is  $40.8 \text{ g m}^{-2} \text{ yr}^{-1}$ , which is overall comparable to the estimate by the  
 584 WaTEM/SEDEM ( $42.5 \text{ g m}^{-2} \text{ yr}^{-1}$ ).



585 ORCHIDEE-C<sub>lateral</sub> reproduces 83% of the inter-site variation of the **observed riverine** sediment  
 586 discharge rates across Europe (Fig. 34b). Simulation of the riverine sediment discharge rate at  
 587 large spatial scale is still a big challenge. It generally needs detailed information on the stream  
 588 flow, geomorphic properties of river channel and the particle composition of the suspended  
 589 sediment (Neitsch et al., 2011). Moreover, the parameters of existing sediment transport models  
 590 usually require recalibration when they are applied to different catchments (Gassman et al.,  
 591 2014; Oeurng et al., 2011; Vigiak et al., 2017). In ORCHIDEE-C<sub>lateral</sub>, the sediment processes in  
 592 river networks are simulated using simple empirical functions and parameters based on a routing  
 593 scheme at a spatial resolution of 0.5° (section 2.2.1). Detailed information about the stream flow  
 594 (e.g. cross-sectional area) and the geomorphic properties of river channels are not represented.  
 595 Sediment discharge in all catchments was simulated using a universal parameter set. This may  
 596 explain why ORCHIDEE-C<sub>lateral</sub> fails to capture the **observed** sediment discharge rates in some  
 597 specific catchments, especially those with relatively small drainage areas (e.g. < 5×10<sup>3</sup> km<sup>2</sup>).



598  
 599 **Figure 34** Comparison between the simulated area-averaged sediment delivery rate from uplands  
 600 to river network from ORCHIDEE-C<sub>lateral</sub> and WaTEM/SEDEM (a), and the comparison between  
 601 observed and simulated annual sediment discharge rates at 221 gauging sites (b). In figure (a),  
 602 the two hollow dots represent the sediment delivery rates at the two catchments in the Apennine  
 603 Peninsula (Fig. S4dS3d). The regression function in figure (a) was obtained based on the values  
 604 of all solid dots, excluding the two hollow dots. In figure (b), the error bar denotes the standard

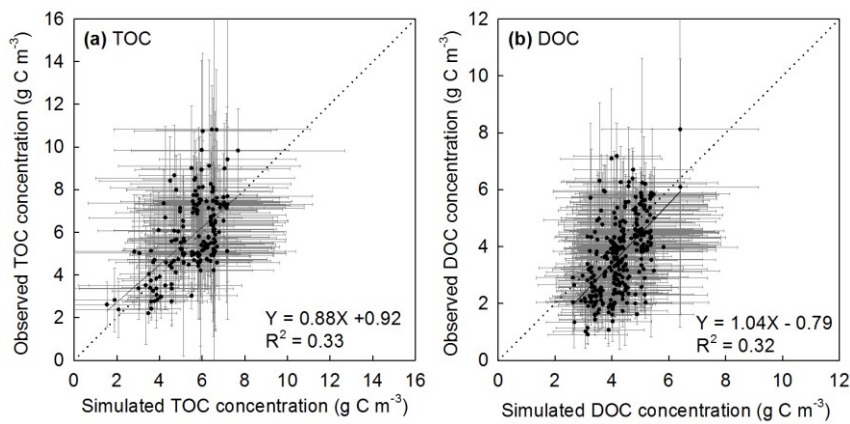
605 deviation of interannual variation. Sources of the observed annual sediment discharge rate in  
606 Table 1.

### 607 **3.1.3 Organic carbon transport**

608 Simulation of the riverine carbon discharge rate at large spatial scale is even a bigger challenge  
609 than simulating sediment discharge, as the riverine carbon discharge is controlled by many  
610 factors, such as upland topsoil SOC concentrations, soil erosion rate, transport and deposition  
611 rate of clay fraction in river channel and on floodplain, and the decomposition of POC in transit  
612 and in aquatic sediments. As described above, the simulated water discharge rate, bankfull flow  
613 and sediment discharge rate are overall comparable to observation (Figs. [23](#) and [34](#)). The  
614 simulated total SOC stock in the top 0-30 cm soil layer in Europe of 107 Pg C is close to the  
615 value extracted from the HWSD database (106 Pg C), but significantly lower than the values  
616 extracted from some other databases, such as the GSDE (249 Pg C), SoilGrids (202 Pg C),  
617 S2017 (148 Pg C) and landGIS (226 Pg C) (Fig. [S8a-S7a](#)). We noticed that the SOC stocks  
618 extracted from these observation-based soil databases show considerable difference (vary from  
619 106 to 249 Pg C), as they have been produced using different clusters of site-level SOC  
620 measurements and different interpolation methods to produce global gridded SOC stocks from  
621 the site-level measurements (Shangguan et al., 2014; Hengl et al., 2014; Sanderman et al., 2017).  
622 Distribution of the simulated SOC stock along the latitude gradients (30° N – 75° N) are overall  
623 comparable to those extracted from the HWSD and S2017 databases (Fig. [S8S7](#)). But even  
624 compared to these two databases, our model still underestimated the SOC stock in southern  
625 Europe (30° N – 41° N).

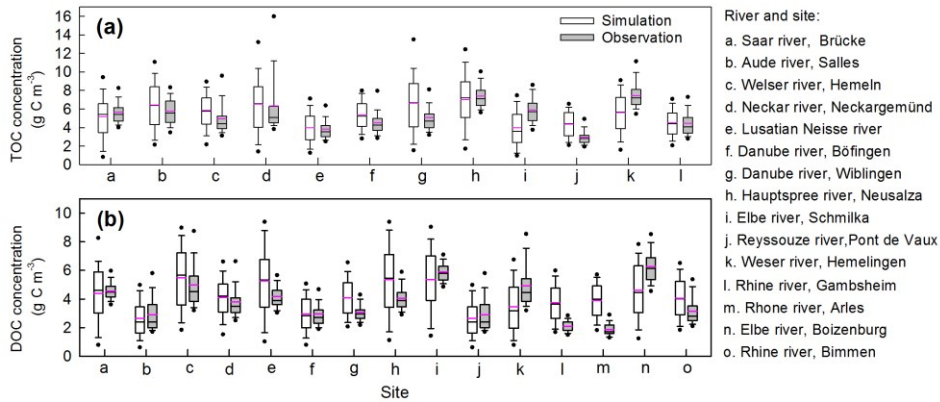
626 Comparison of the simulated concentrations of riverine organic carbon and the observations  
627 obtained from the GLORICH database (Hartmann et al., 2019) indicates that our model can  
628 basically capture the TOC and DOC concentrations in European rivers (Figs [4-5](#), [S96](#), [S8](#) and  
629 [S10S9](#)). The simulation results explain 34% and 32% of the inter-site variation of the observed  
630 TOC and DOC concentrations, respectively (Fig. [45](#)). For major European rivers, such as the  
631 Rhine, Elbe, Danube, Spree and Weser, the simulated long-term average TOC and DOC  
632 concentrations are overall close to the observations (Figs. [5](#), [S96](#), [S8](#) and [S10S9](#)). But for the  
633 Rhone river in southern France, the DOC concentrations have been systematically overestimated  
634 by more than 50% (Figs. [56](#) and [S10mS9m](#)). In addition, both simulated and observed TOC and

635 DOC concentrations show drastic temporal (both seasonal and interannual) variations (Figs 4,  
636 S9S8 and S10S9). Our model seems to have overestimated the temporal variation of TOC and  
637 especially DOC concentrations (Figs. S9S8 and S10S9). Nonetheless, the simulated temporal  
638 variation of TOC and DOC discharge rates are overall comparable to the observation (Figs.  
639 S11S10 and S12S11), as our model can well capture the magnitude and temporal variation of  
640 riverine water discharge rates.

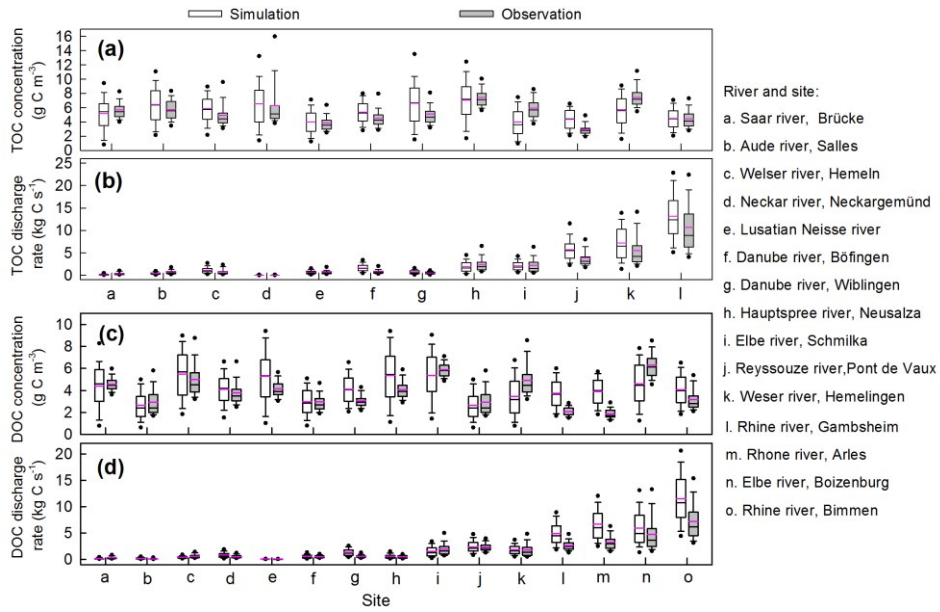


642 **Figure 45** Comparison between the observed and simulated riverine TOC (a, POC+DOC) and  
643 DOC (b) concentrations. The dot and error bar denote the mean and standard deviation at each  
644 gauging site, respectively. Note that the mean and standard deviation of the simulated  
645 concentrations at each site are calculated based on the monthly average value, but the mean and  
646 standard deviation of the observed concentrations are based on instantaneous observation.

647

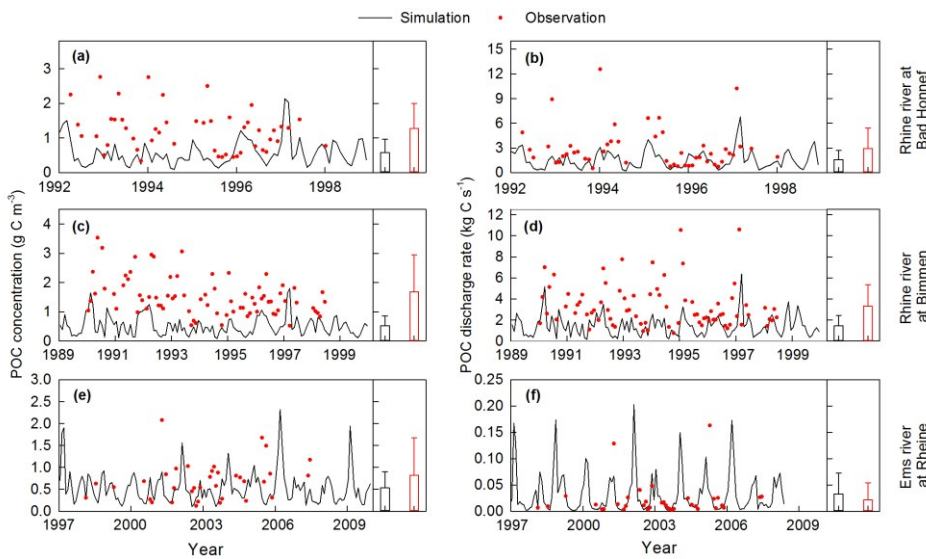


648



649 **Figure 56** Comparison between the observed and simulated concentrations of total organic  
650 carbon (TOC, a) and dissolved organic carbon (DOC, b) in river flows-, as well as the discharge  
651 rates of riverine TOC and DOC. The black and pink lines in each box denote the median and  
652 mean value, respectively. Box boundaries show the 25<sup>th</sup> and 75<sup>th</sup> percentiles, whiskers denote the  
653 10<sup>th</sup> and 90<sup>th</sup> percentiles, the dots below and above each box denote the 5<sup>th</sup> and 95<sup>th</sup>  
654 percentiles, respectively.

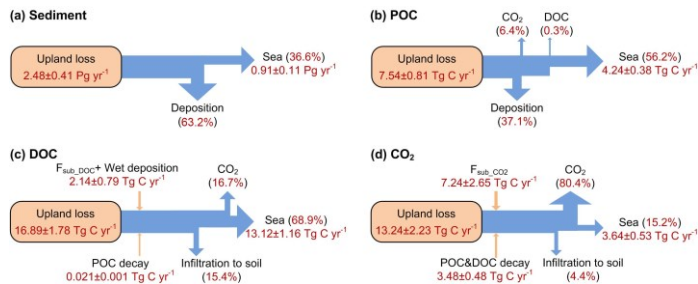
655 In Europe, the GLORICH database only provides POC concentrations measured at three gauging  
 656 stations in northwestern Germany (Figs. 6, S4d7, S3d). The simulated POC concentrations and  
 657 discharge rates in the Ems river at Rheine are overall comparable to the observation (Figs.  
 658 6e7e,f). However, at the two gauging sites at the river Rhine, the POC concentrations have been  
 659 significantly underestimated (Figs. 6a7a-d). We noticed that the stream routing scheme of Rhine  
 660 catchment at 0.5° obtained from the forcing data STN-30p (Vörösmarty et al., 2000) differs  
 661 significantly from the stream routing scheme extracted based on high resolution (3") DEM (Fig.  
 662 S7S6). Thus, besides the errors in simulated SOC stocks, soil erosion rate, stream discharge rate,  
 663 and sediment transport and deposition rate, the inaccurate stream routing scheme used in this  
 664 study might also be an important reason for the underestimation of POC concentration in Rhine  
 665 river.



666  
 667 **Figure 67** Comparison between observed (instantaneous measurements) and simulated (monthly  
 668 average values) riverine POC concentrations and POC discharge rates at three gauging sites. The  
 669 histograms and error bars denote the means and standard deviations of POC concentrations,  
 670 respectively. Long-term average water discharge rates at Bad Honnef, Bimmen and Rheine  
 671 during the observation periods are 2023, 2100 and 80 m<sup>3</sup> s<sup>-1</sup>, respectively.

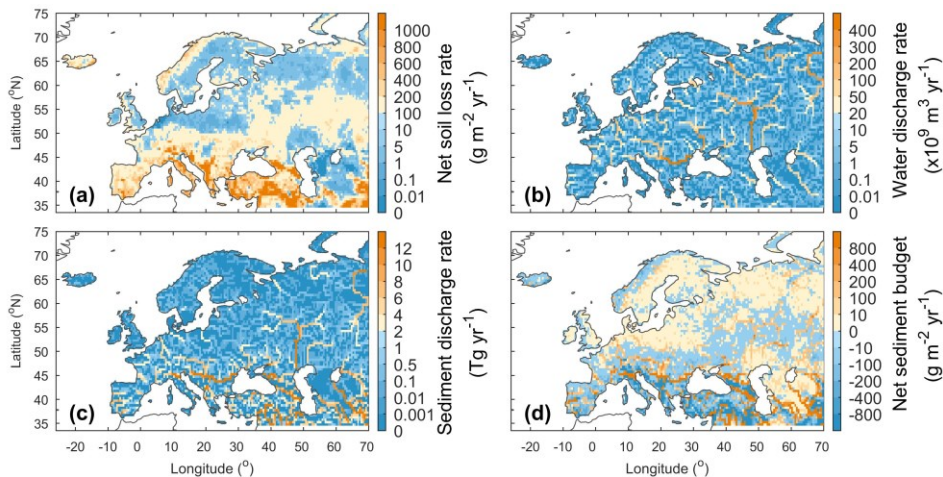
### 672 3.2 Lateral carbon transfers in Europe

673 Based on our simulation results, the average annual sediment delivery from upland to the river  
674 network caused by water erosion in Europe (-30W– 70E, 34N-75N) during 1901-2014 is  $2.8 \pm 0.4$   
675  $\text{Pg yr}^{-1}$  (Fig. 7a8a). From Northern to Southern Europe, the sediment delivery rate from upland to  
676 river increase from less than  $1.0 \text{ g m}^{-2} \text{ yr}^{-1}$  in the Scandinavia Peninsula, which is covered by  
677 mature boreal forests (Fig. S13aS12a), and in the Northern European Plain to more than  $600 \text{ g m}^{-2}$   
678  $\text{yr}^{-1}$  in the mountainous regions of the Apennine Peninsula, Balkan Peninsula and the Middle  
679 East (Figs. 8a, S14a). ~~The Caucasus is mainly covered by ice and bare rock (Fig. S13), thus the~~  
680 ~~sediment delivery rate in this region is also very low.~~9a. S13a). In total across Europe, 63.2%  
681 ( $1.8 \pm 0.2 \text{ Pg yr}^{-1}$ ) of the sediment delivered into river network is deposited in river channels and  
682 floodplains, and the remaining 36.8% ( $1.0 \pm 0.1 \text{ Pg yr}^{-1}$ ) is exported to the sea (Fig. 7a8a).  
683 Generally, large rivers, like Danube, Volga, and Ob rivers, carry more sediment to the sea than  
684 small rivers (Figs. 8b9b, c). But several relatively small rivers in the Middle East and the Po river  
685 in northern Italy also carry similarly large amount of sediment to the sea, as the upland soil  
686 erosion rates are very high ( $> 200 \text{ g m}^{-2} \text{ yr}^{-1}$ ) in these catchments (Figs. 8a9a, c). Spatial  
687 distribution of the sediment deposition is controlled by the stream routing scheme and the spatial  
688 distribution of floodplains (Fig. 9b10b). In Northern and Central Europe, the area-averaged  
689 sediment deposition rates (i.e. amount of annual sediment deposition /area of  $0.5^\circ \times 0.5^\circ$  grid cell)  
690 in river channels and floodplains are mostly less than  $100.0 \text{ g m}^{-2} \text{ yr}^{-1}$  (Fig. 8d9d). In the  
691 downstream part of the Danube, Po and several rivers in the Middle East, the sediment  
692 deposition rate can exceed  $800.0 \text{ g m}^{-2} \text{ yr}^{-1}$ . From 1901 to 1960s, the annual total sediment  
693 delivery from uplands to the whole river network of Europe declined significantly ( $p < 0.01$ ,  
694 independent sample t-test) from about  $3.0 \text{ Pg yr}^{-1}$  to about  $2.3 \text{ Pg yr}^{-1}$  (Fig. S15aS14a). From  
695 1960 to 2014, the annual sediment delivery rate did not show a significant trend, but revealed  
696 large interannual variations.



697

698 **Figure 78** Averaged annual lateral redistribution rate of sediment (a), POC (b) and  
 699  $\text{CO}_2$  (d) in Europe for the period 1901-2014.  $F_{\text{sub\_DOC}}$  and  $F_{\text{sub\_CO}_2}$  are the DOC and  $\text{CO}_2$  inputs  
 700 from floodplain soil (originated from the decomposition of submerged litter and soil carbon) to  
 701 the overlying flooding water, respectively.



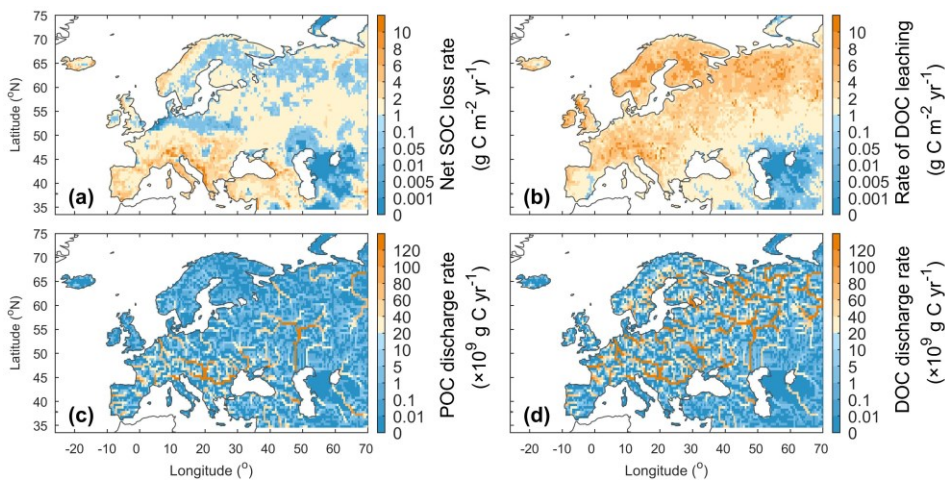
702

703 **Figure 82** Averaged annual lateral redistribution rate of water and sediment in Europe during  
 704 1901-2014. (a) Annual sediment delivery rate from upland to river network; (b) annual water  
 705 discharge rate; (c) annual sediment discharge rate and (d) annual net sediment budget in each  
 706  $0.5^\circ \times 0.5^\circ$  grid cell. In figure d, the positive and negative values denote net gain and net loss of  
 707 sediment, respectively.

708 Along with soil erosion and sediment transport, the average annual POC delivery from upland to  
 709 river network in the whole Europe during 1901-2014 is  $10.1 \pm 1.1 \text{ Tg C yr}^{-1}$  (Fig. 7b8b). 41.0% of



710 the POC delivered into the river network is deposited in river channels and floodplains, 2.9% is  
 711 decomposed during transport, and the remaining 56.1% is exported to the sea. Spatial patterns of  
 712 the area-averaged SOC delivery rate and POC discharge rate basically follow that of sediment  
 713 (Fig. 9a10a, c). Although the sediment discharge rates in some rivers in the Middle East can be  
 714 as high as that in the Danube or Volga river (Fig. 8e9c), the POC delivery rates in these rivers  
 715 are much smaller than in the larger ones (Fig. 9e10c). This is mainly due to the lower SOC  
 716 stocks in the Middle East compared to those found in the Danube and Volga catchments (Fig.  
 717 S8S7). We also note that different from the sediment delivery, the annual total POC delivery  
 718 from upland to river network in Europe did not show a significant declining trend from 1901 to  
 719 1960s (Fig. S15bS14b). The increase in SOC stock (Fig. S15eS14c) may have partially offset the  
 720 decline in sediment delivery rate.



721  
 722 **Figure 910** Averaged annual lateral redistribution rate of organic carbon in Europe during 1901-  
 723 2014. (a) Annual SOC delivery rate from upland to river network; (b) annual DOC leaching rate;  
 724 (c) annual POC discharge rate and (d) annual DOC discharge rate.

725 Leaching results in an average annual DOC input of  $13.5 \pm 1.5$  Tg C yr<sup>-1</sup> from soil to the river  
 726 network in Europe, and the *in-situ* DOC production caused by wet deposition and the  
 727 decomposition of riverine POC and submerged litter and soil organic carbon under flooding  
 728 waters amounts to  $2.2 \pm 0.7$  Tg C yr<sup>-1</sup> (Fig. 7e8c). 28.1% of the total riverine DOC is then

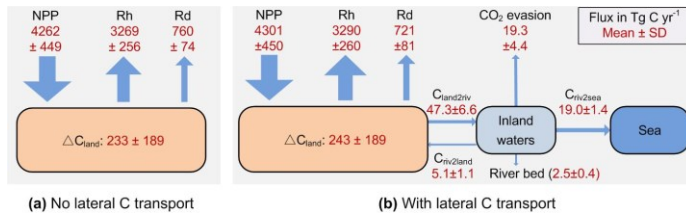


729 infiltrating into the floodplain soils, 12.9% is decomposed during riverine transport, and the  
730 remaining 59.0% is exported to the sea. The spatial distribution of the DOC leaching rate is very  
731 different from that of POC (Fig. 9b10b). From North-western Europe to Southeast Europe and  
732 the Middle East, the DOC leaching rates decrease from over 6 g C m<sup>-2</sup> yr<sup>-1</sup> to less than 1.0 g C m<sup>-2</sup>  
733 yr<sup>-1</sup>. DOC discharge rates in major European rivers, such as Rhine, Danube, Volga, Elbe and  
734 Ob, are mostly higher than 100 Tg C yr<sup>-1</sup> (Fig. 9a10d). Comparatively, the DOC discharge rates  
735 in Southern Europe and the Middle East are significantly lower (<60 Tg C yr<sup>-1</sup>).

736 The average annual leaching rate of CO<sub>2</sub> sourced from the decomposition of upland litter and  
737 soil organic carbon (incl. DOC) in the whole Europe is 14.3±2.2 Tg C yr<sup>-1</sup> (Fig. 7a8a).  
738 Decomposition of the submerged litter and organic carbon in floodplains and the decomposition  
739 of riverine POC and DOC add an *in-situ* CO<sub>2</sub> production amounting to 7.5±2.7 Tg C yr<sup>-1</sup> and  
740 4.1±0.5 Tg C yr<sup>-1</sup>, respectively. Most of this CO<sub>2</sub> (80.2%) feeding stream waters is then released  
741 back to the atmosphere quickly, in such a way that only 15.8% of the CO<sub>2</sub> is exported to the sea,  
742 and 4.0% is infiltrated into the floodplain soils.

### 743 3.3 Implications for the terrestrial C budget of Europe

744 Representing the lateral carbon transport in LSM is helpful to estimate the terrestrial carbon  
745 cycle more accurately. From the year 1901 to 2014, soil erosion and leaching combined resulted  
746 in a 5.4 Pg loss of terrestrial carbon to the European river network, this amount corresponding to  
747 about 5% of the total SOC stock (106 Pg C, Fig. 8aS7a) in the 0-30 cm soil layer. The average  
748 annual total delivery of organic carbon (POC+DOC) during the same period is 47.3±6.6 Tg C yr<sup>-1</sup>  
749 (Fig. 78), which is about 4.7% of the net ecosystem production (NEP (993±255 Tg C yr<sup>-1</sup>),  
750 defined as the difference between the vegetation primary production (NPP) and the soil  
751 heterotrophic respiration (Rh) due to the decomposition of litter and soil organic matter, i.e.  
752 NEP=NPP-Rh), and 19.2% of the net biome production (NBP (243±189 Tg C yr<sup>-1</sup>), defined as  
753 the difference between NEP and the land carbon loss (Rd) due to the additional disturbances (e.g.  
754 harvest, land cover change, and soil erosion and leaching, i.e. NBP=NEP-Rd-DOC and POC to  
755 river) (Fig. 10b11b). The annual total export of carbon to the sea surrounding Europe is 19.0±1.4  
756 Tg C yr<sup>-1</sup>, which amounts to 1.9% and 8.7% of the NEE and NBP, respectively.



757

758 **Figure 1011** The simulated average annual carbon budget of the terrestrial ecosystem in Europe  
 759 during the 1901-2014 when the lateral carbon transport is ignored (a) and considered (b). All  
 760 fluxes are presented as mean  $\pm$  standard deviation. NPP is the net primary production. Rh and Rd  
 761 are the heterotrophic respiration and the respiration due to disturbances like harvest and land  
 762 cover change, respectively.  $\Delta C_{land}$  is the average annual changes of the total land carbon stock.  
 763 Percentage following each of these changes in blue is the average annual relative changes of the  
 764 corresponding carbon pool.  $C_{land2riv}$ ,  $C_{riv2land}$  and  $C_{riv2sea}$  are the average annual carbon fluxes  
 765 from land to inland waters, from inland waters to floodplains and from inland waters to the sea,  
 766 respectively. SD is the standard deviation.

767 Besides direct transfers of organic carbon from soil to aquatic systems, the lateral transport of  
 768 water, sediment and carbon can also affect the land carbon budget through several indirect ways.  
 769 First, the lateral redistribution of surface runoff can affect the land carbon budget by altering soil  
 770 wetness. Our simulation results reveal that the lateral redistribution of runoff can significantly  
 771 change local soil wetness, especially in floodplains (Fig. S14bS13b), where the increase in soil  
 772 wetness can be larger than 10% (Fig. S17bS16b). Soil wetness is a key controlling factor of plant  
 773 photosynthesis (Knapp et al., 2001; Stocker et al., 2019; Xu et al., 2013). Benefiting from the  
 774 increase in soil wetness, the NPP in many grid cells with a large area of floodplain has increased  
 775 by more than 5% (Fig. 40b11b), although the NPP over the whole Europe only increased by 1%  
 776 (Fig. 4011). Changes in soil wetness can further alter soil temperature (Fig. S17aS16a). As soil  
 777 wetness and temperature are the two most important controlling factors of organic matter  
 778 decomposition, the lateral redistribution of runoff can affect local land carbon budget by  
 779 changing the Rh. Moreover, in ORCHIDEE-C<sub>lateral</sub>, the turnover times of litter and SOC under  
 780 flooding waters (assumed to experience anaerobic condition) are set to be one third of the litter  
 781 and SOC turnover times in upland soil (Reddy & Patrick Jr, 1975; Neckles & Neill, 1994;

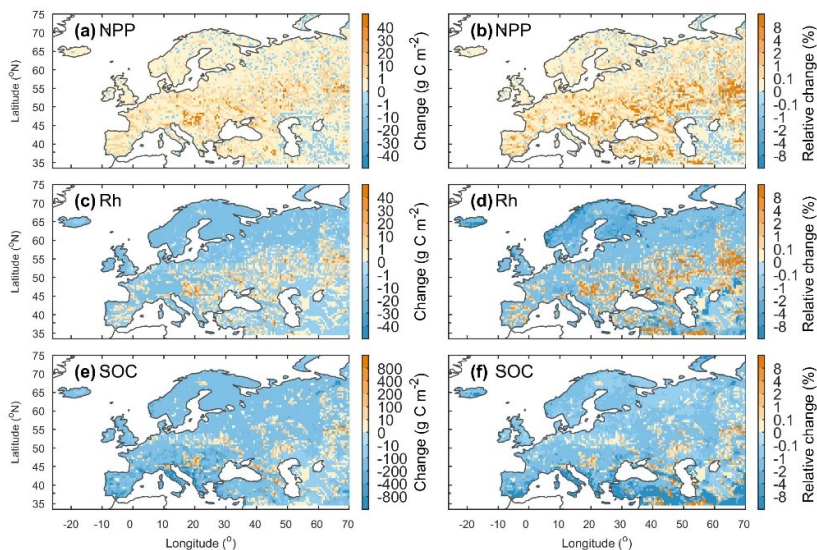
782 Lauerwald et al., 2017). Accounting for flooding thus decreases the decomposition rate of litter  
783 and SOC stored in floodplain soils.

784 Second, soil erosion and sediment deposition can affect land carbon budget by altering the  
785 vertical distribution of litter and soil organic carbon. At the net erosion sites of the uplands, the  
786 loss of surface soil results in a part of the belowground litter and SOC that were originally stored  
787 in deeper soil layers emerging to the surface soil layers, and also results in a fraction of the  
788 belowground litter becoming the aboveground litter. In the floodplains, the newly deposited  
789 sediment becomes part of the surface soil layer, and the belowground litter and SOC in the  
790 original surface soil layer is transferred down to the deeper soil layers. As the temperatures and  
791 fresh organic matter inputs (sourced from the aboveground litterfall and dead roots), which can  
792 impact SOC decomposition rates through the priming effect (Guenet et al., 2016; Guenet et al.,  
793 2010), in different soil layers are different, changes in the vertical distribution of belowground  
794 litter and SOC can therefore lead to changes in the overall decomposition rate of the organic  
795 matter in the whole soil column.

796 Third, soil aggregates mostly break down during soil erosion and sediment transport, the riverine  
797 POC thus loses part of its physical protection from decomposition (Hu and Kuhn, 2016; Lal,  
798 2003). Some modelling studies have assumed that at least 20% of the eroded SOC would be  
799 decomposed during the soil erosion and transport processes (Lal, 2003, 2004; Zhang et al.,  
800 2014). However, the estimation by Smith et al. (2001) using a conceptual mass balance model  
801 suggest that only a tiny fraction of the eroded POC is decomposed and released as CO<sub>2</sub> to the  
802 atmosphere. Using laboratory rainfall-simulation experiments, van Hemelryck et al. (2010)  
803 estimated a 2%-12% mineralization of the eroded SOC from a loess soil, and Wang et al. (2014)  
804 estimated a mineralization of only 1.5%. In ORCHIDEE-C<sub>lateral</sub>, the passive SOC pool is  
805 regarded as the SOC associated to soil minerals and protected by soil aggregates. The turnover  
806 time of the passive POC in river stream and flooding waters is assumed to be same to that of the  
807 active POC (0.3 year). Our simulation results suggest that the fraction of total riverine POC that  
808 is decomposed during the lateral transport from uplands to the sea is 2.9% in Europe (Fig. 7b8b),  
809 which is larger than the POC decomposition fraction (0.9%) when the turnover time of the  
810 passive POC in rivers is assumed to be same to that of the passive POC (i.e. no soil aggregates  
811 break down). The acceleration of POC decomposition rate due to the breakdown of soil

812 aggregates can thus slightly affect the estimate of the regional land-atmosphere carbon flux.  
813 Moreover, the riverine POC and DOC can be transported over a long distance and finally settle  
814 or infiltrate in floodplains or river channels (especially the Estuarine deltas) where the local  
815 environmental conditions might be quite different from those encountered in the uplands from  
816 where these C pools originate. These changes in environmental conditions can affect the  
817 decomposition rate of the laterally redistributed organic carbon (Abril et al., 2002).

818 Comparison between the simulation results from ORCHIDEE-C<sub>lateral</sub> with activated and  
819 deactivated erosion and river routing modules indicate that ignoring lateral carbon transport  
820 processes in LSM may lead to significant biases in the simulated land carbon budget (Figs. [+011](#)  
821 and [S15S14](#)). Although the omission of lateral carbon transport in ORCHIDEE-C<sub>lateral</sub> only  
822 resulted in a 1% decrease in simulated average annual total NPP in Europe during 1901-2014  
823 and a 1% increase of annual total Rh, the annual total NBP (=NEP-Rd-DOC and POC to river)  
824 is overestimated by 4.5%. Over the same period, the lateral carbon transport only induced a  
825 0.09% decrease in the total SOC and DOC stock in Europe (Fig. [S16eS15c](#)), but their spatial  
826 distribution was significantly altered (Figs. [+e12e,f](#)). For instance, in some mountainous  
827 regions, the soil erosion induced a reduction of the SOC stock by more than 8%. On the contrary,  
828 the sediment and POC deposition in some floodplains led to an increase in SOC stock by more  
829 than 8% (Fig. [+f12f](#)).



830

831 **Figure 11** Changes (first column) and relative changes (second column) of the net primary  
 832 production (NPP), heterotrophic respiration (Rh) and total soil organic carbon (SOC, 0-2 m) in  
 833 Europe due to the lateral carbon transport during 1901-2014. For each variable, the change is  
 834 calculated as  $C_{lat} - C_{nolat}$ , where  $C_{lat}$  and  $C_{nolat}$  are the carbon fluxes or stocks when lateral carbon  
 835 transport is considered and ignored, respectively. The relative changes is calculated as  $(C_{lat} -$   
 836  $C_{nolat}) / C_{nolat} \times 100\%$ .

837 Consistent with previous studies (Stallard, 1998; Smith et al., 2001; Hoffmann et al., 2013), our  
 838 simulation results reveal the importance of sediment deposition in floodplains for the overall  
 839 SOC budget. From 1901 to 2014, erosion and leaching over Europe totally induced a loss of 3.03  
 840 Pg organic carbon (POC+DOC) from uplands to the river network, and only 0.65 Pg of this  
 841 carbon was redeposited onto the floodplains. The total stock of soil organic carbon in Europe  
 842 thus should have decreased by 2.38 Pg C. However, due to the decrease in decomposition rate of  
 843 the buried organic carbon (including in-situ and ex-situ carbon) in floodplain soils, the total stock  
 844 of soil organic carbon in Europe only decreased by 0.91 Pg C. Floodplains in Europe have totally  
 845 protected 2.12 (= 3.03 - 0.91) Pg soil organic carbon from been transported to the sea or be  
 846 released to the atmosphere in forms of CO<sub>2</sub>. Although the sequestration of organic carbon in  
 847 floodplains cannot make up all of the soil organic carbon (POC+DOC) loss, the increased

848 organic carbon stock in floodplains (2.12 Pg C) is much higher than the soil POC loss (0.86 Pg  
849 C) induced by soil erosion.

### 850 **3.4 Uncertainties and future work**

851 In the present version of ORCHIDEE-Clateral, the lateral transfers of sediment and carbon is  
852 simulated using a simplified scheme, due to the fragmented nature of large-scale forcing (e.g.  
853 geomorphic properties of the river channel) and validation data (e.g. continuous sediment and  
854 carbon concentration data in river streams and deposition/erosion rates in river channels). We  
855 recognize that this simplification induces significant uncertainties in model outputs, especially  
856 regarding changes in lateral sediment and particulate carbon transfers under climate change and  
857 direct human perturbations. Several physics-based algorithms have been proposed to accurately  
858 calculate the *TC* of stream flows (Arnold et al., 1995; Molinas and Wu, 2001; Nearing et al.,  
859 1989). These algorithms mostly require detailed information about the stream power (e.g. flow  
860 speed and depth), geomorphic properties of the river channel (e.g. slope and hydraulic radius)  
861 and the physical properties of the sediment particles (e.g. median grain size) (Neitsch et al.,  
862 2011). They are good predictors to estimate *TC* in rivers with detailed observation data on local  
863 stream, soil, geomorphic properties. Unfortunately, it is not practical to implement those  
864 algorithms in ORCHIDEE-C<sub>lateral</sub> due to the lack of appropriate forcing data at large scale as well  
865 as the relatively rough representation of stream flow dynamics compared to hydrological models  
866 for small basins. For example, runoff and sediment from all headwater basins in one 0.5° grid  
867 cell of ORCHIDEE-C<sub>lateral</sub> are assumed to flow into one single virtual river channel. Although  
868 the total river surface area in each grid cell is represented (obtained from forcing file (Table 1),  
869 Lauerwald et al., 2015), the length, width and depth of the river channel are unknown.  
870 Furthermore, in reality, there can be multiple river channels in the area represented by each grid  
871 cell, and these channels might flow to different directions.

872 We also noticed that previous studies have derived empirical functions of upstream drainage area  
873 (e.g. Luo et al., 2017) or upstream runoff (e.g. Yamazaki et al., 2011) to calculate the river width  
874 and depth, allowing to simulate the water flow in the river channel using physically-based  
875 algorithms. Unfortunately, to obtain a good fit of the simulated river discharges against  
876 observations, the parameters in the empirical functions for calculating river width and depth  
877 generally need to be calibrated separately for each catchment (Luo et al., 2017), an approach that

878 is incompatible with large-scale simulations like those performed here. Without such calibration,  
879 the simulated geometrical properties of the river channel and runoff are prone to large  
880 uncertainties, thus rendering the simulation of sediment transport at continental or global scale  
881 using physically-based algorithms a more challenging task. Given the difficulty to simulate the  
882 detailed hydraulic dynamics of the stream flow at large spatial scale, we thus apply a simple  
883 approach ~~described below~~(Eq. 8) to calculate the sediment transport capacity. Overall, we  
884 encourage future studies to produce large-scale databases on the geomorphic properties of global  
885 river channels (e.g. river depth and width) and to develop large-scale sediment transport models  
886 which can give a capable of producing more realistic and accurate simulations of sediment  
887 deposition, re-detachment and transport processes, as well as including the exchanges of water,  
888 sediment and carbon between river stream and floodplains.

889 The simulation of the soil DOC dynamics and leaching in our model need to be further improved  
890 to better simulate the seasonal variation of riverine DOC and TOC concentrations. The  
891 concentration of soil DOC and the DOC decomposition rate during the lateral transport process  
892 in the river network are the two key factors controlling DOC concentration in river flow. As  
893 only a small fraction (< 20%) of the riverine DOC is decomposed during lateral transport (Fig.  
894 78), the overestimated (Fig. 56) seasonal amplitude in riverine DOC (and TOC) concentrations is  
895 likely caused by the uncertainties in the simulated seasonal dynamics of the leached soil DOC.  
896 The current scheme used in our model for simulating soil DOC dynamics has been calibrated  
897 against observed DOC concentrations at several sites in Europe (Camino-Serrano et al., 2018).  
898 Although the calibrated model can overall capture the average concentrations of soil DOC, it is  
899 not able to fully capture the temporal dynamics of DOC concentrations (Camino-Serrano et al.,  
900 2018). Given this, it is necessary to collect additional observation data on the seasonal dynamics  
901 of soil DOC concentration to further calibrate the soil DOC model. In addition, averaged over  
902 the various DOC and SOC pools we distinguish in the soils, DOC represents a much more  
903 reactive fraction of soil carbon (with a turnover time of several days to a few months) than SOC  
904 (with a turnover time of decades to thousands of years). Therefore, soil DOC concentrations  
905 experience large seasonal variations, while SOC concentrations generally are much more stable  
906 and show very limited seasonal dynamics. Overall, seasonal variations in riverine POC  
907 concentrations are mainly controlled by the seasonal dynamics of soil erosion rates, rather than

908 by the seasonal SOC dynamics, which explains a partial decoupling in the behavior of POC  
909 compared to that of DOC.

910 Although most processes related to lateral carbon transport have been represented in  
911 ORCHIDEE-C<sub>lateral</sub>, there are still omitted processes and large uncertainties in our model. For  
912 example, many studies suggest that a substantial portion of the eroded sediment and carbon is  
913 deposited downhill at adjacent lowlands as colluviums, rather than exported to the river (Berhe et  
914 al., 2007; Smith et al., 2001; Hoffmann et al., 2013; Wang et al., 2010). As the deposition of  
915 sediment and carbon within headwater basins can also significantly alter the vertical SOC profile  
916 and soil micro-environments (e.g. soil moisture, aeration and density) (Doetterl et al., 2016;  
917 Gregorich et al., 1998; Wang et al., 2015; Zhang et al., 2016), omission of this process may  
918 result in uncertainties in the simulated vegetation production and SOC decomposition. In  
919 addition, the impact of artificial dams and reservoirs on riverine sediment and carbon fluxes is  
920 also not represented in our model. Construction of dams generally leads to increased water  
921 residence time, nutrient retention, and sediment and carbon trapping in the impounded reservoir  
922 (Habersack et al., 2016; Maavara et al., 2017), and can also affect the downstream flooding  
923 regime and frequency (Mei et al., 2016; Timpe and Kaplan, 2017). Estimation by Maavara et al.  
924 (2017) suggests that the organic carbon trapped or mineralized in global artificial reservoirs is  
925 about 13% of the total organic carbon carried by global rivers to the oceans. To more accurately  
926 simulate the lateral carbon transport, we plan to include the soil and carbon redistribution within  
927 headwater basins and the effects of dams and reservoirs on riverine sediment and carbon fluxes  
928 into our model in the near future.

929 The effects of lateral redistribution of water and sediment on vegetation productivity has not  
930 been fully represented in our model. As shown above, our model is able to represent the impacts  
931 of lateral water redistribution on vegetation productivity through modifying local soil wetness  
932 (Figs. 4+12 and S17S16). However, in addition to modifying soil wetness, many studies have  
933 indicated that the soil erosion and sediment deposition can affect vegetation productivity by  
934 modifying soil nutrient (e.g. nitrogen (N) and phosphorus (P)) availability (Bakker et al., 2004;  
935 Borrelli et al., 2018; Quine, 2002; Quinton et al., 2010). Recently, terrestrial N and P cycles have  
936 already been incorporated into another branch of ORCHIDEE (i.e. the ORCHIDEE-CNP  
937 developed by Goll et al., 2017). By coupling our new branch and ORCHIDEE-CNP, it will be



938 possible to develop a more comprehensive LSM that can also simulate the effects of lateral N  
939 and P redistribution on vegetation productivity.

940 Although soils are the major source of riverine organic carbon, domestic, agricultural and  
941 industrial wastes, as well as river-borne phytoplankton can also make significant contributions  
942 (Abril et al., 2002; Meybeck, 1993; Hoffmann et al., 2020). Moreover, previous studies have  
943 shown that sewage generally contains highly labile POC while most of the aquatic production is  
944 generally mineralized within a short time (Abril et al., 2002; Caffrey et al., 1998). Omission of  
945 organic carbon inputs from manure and sewage could potentially lead to an underestimation of  
946 CO<sub>2</sub> evasion from the European river network. Inclusion of these additional carbon sources  
947 should thus help improve simulation of aquatic CO<sub>2</sub> evasion.

948 Uncertainties in our simulation results also stem from the forcing data (Table 1) applied in our  
949 model. The routing scheme of water, sediment and carbon is driven by a map of stream flow  
950 direction at 0.5° spatial resolution (Guimberteau et al., 2012). Comparison between this flow  
951 direction map and the flow direction map derived based on high resolution (3") DEM show  
952 discrepancies between the two river flow networks (Fig. [S7S6](#)). As the flow direction directly  
953 determines the area of each catchment and the route of river flows, errors in forcing data of flow  
954 direction may thus induce uncertainties in the simulated riverine water, sediment and carbon  
955 discharges. Land-cover maps are another source of uncertainty. For instance, croplands generally  
956 experience significantly larger soil erosion rates than grasslands and forests (Borrelli et al., 2017;  
957 Nunes et al., 2011; Zhang et al., 2020). However, croplands in ORCHIDEE are only represented  
958 in a simplified way by segmenting them into C3 and C4 crops based on their photosynthesis  
959 characteristics. Therefore, our simulations based on land cover data with only two broad groups  
960 of crop might not be able to fully capture the seasonal dynamics of planting, canopy growth rate  
961 and harvesting for all crop types. Furthermore, the effects of soil conservation practices, which  
962 would decrease erosion rates, are ignored in our model. Panagos et al. (2015) have shown that  
963 contour farming, stone wall and grass margin techniques have been applied in Europe reduce the  
964 risk of soil erosion. However, these soil conservation practices only reduce the average erosion  
965 rate in European Union by 3%. Excluding soil conservation practices thus should have limited  
966 impact in our simulation results.

967 Further model calibration, evaluation and development is necessary for improving our model.  
968 Due to the limitation of observation data, we calibrated the parameters controlling sediment  
969 transport, deposition and re-detachment (i.e.  $\omega$ ,  $C_{rivdep}$ ,  $C_{flddep}$ ,  $C_{ebed}$  and  $C_{ebank}$  in Table S1) in  
970 stream and flooding reservoirs only against the observed sediment yield. Even though our model  
971 can overall capture the lateral transfers of sediment and carbon in many rivers in central and  
972 northern Europe, more observation data are crucially needed to further evaluate the performance  
973 of our model, in particular in southern Europe. In addition, it is still unknown whether our model  
974 can satisfactorily simulate intermediate processes such as sediment deposition in river channels  
975 and floodplains, as well as the rate of river channel erosion. It is also unknown whether our  
976 model would perform satisfactorily in regions with very different climates than Europe such as  
977 the tropical region. Thus, in the future, an important aim will be to further calibrate our model  
978 against more detailed observation data (e.g. sediment deposition rate in river channels and  
979 floodplains) and extend the model application to regions of contrasting climate, vegetation and  
980 topography. Moreover, the GLORICH database (Hartmann et al., 2019) only provides  
981 instantaneous observations of riverine organic carbon concentrations and it is therefore difficult  
982 to evaluate the model's ability to reproduce temporal trends. Therefore, future modelling efforts  
983 should be combined with data mining efforts targeting the collection of continuous (e.g. daily)  
984 and long-term observational data of organic carbon content and fluxes in streams and rivers.

985

## 986 **Conclusions**

987 By merging ORCHILEAK (Lauerwald et al., 2017) and an upgraded version of ORCHIDEE-  
988 MUSLE (Zhang et al., 2020) for the simulation of DOC and POC from land to sea, respectively,  
989 we developed ORCHIDEE- $C_{lateral}$ , a new branch of the ORCHIDEE LSM. ORCHIDEE- $C_{lateral}$   
990 simulates the large-scale lateral transport of water, sediment, POC, DOC and CO<sub>2</sub> from uplands  
991 to the sea through river networks, the deposition of sediment and POC in river channels and  
992 floodplains, the decomposition POC and DOC during fluvial transport and the CO<sub>2</sub> evasion to  
993 the atmosphere, as well as the changes in soil wetness and vertical SOC profiles due to the lateral  
994 redistribution of water, sediment and carbon.

995 Evaluation using observation data from European rivers indicate that ORCHIDEE- $C_{lateral}$  can  
996 satisfactorily reproduce the observed riverine discharges of water and sediment, bankfull flows

997 and organic carbon concentrations in river flows. Application of ORCHIDEE-C<sub>lateral</sub> to the entire  
998 European river network from 1901 to 2014 reveals that the average annual total carbon delivery  
999 to streams and rivers amounts to  $47.3 \pm 6.6 \text{ Tg C yr}^{-1}$ , which corresponds to about 4.7% of total  
1000 NEP and 19.2% of the total NBP of terrestrial ecosystems in Europe. The lateral transfer of  
1001 water, sediment and carbon can affect the land carbon dynamics through several different  
1002 mechanisms. Besides directly inducing a spatial redistribution of organic carbon, it can also  
1003 affect the regional land carbon budget by altering vertical SOC profiles, as well as the soil  
1004 wetness and soil temperature, which in turn impact vegetation production and the decomposition  
1005 of soil organic carbon. Overall, omission of lateral carbon transport in ORCHIDEE potentially  
1006 results in an underestimation of the annual mean NBP in Europe of 4.5%. In regions  
1007 experiencing high soil erosion or high sediment deposition rate, the lateral carbon transport also  
1008 changes total SOC stock significantly, by more than 8%.

1009 We recognize that ORCHIDEE-C<sub>lateral</sub> is still entailed with several limitations and significant  
1010 uncertainties. To address those, we plan to enhance our model with additional processes, such as  
1011 sediment deposition at downhills or the regulation of lateral transport by dams and reservoirs.  
1012 We also plan to calibrate and evaluate further our model by extending the observational dataset  
1013 to regions outside Europe.

1014

1015 **Code and data availability**

1016 The source code of ORCHIDEE-Clateral model developed in this study is available online  
1017 (<https://doi.org/10.14768/f2f5df9f-26da-4618-b69c-911f17d7e2ed>) from 22 July, 2019. All  
1018 forcing and validation data used in this study are publicly available online. The specific sources  
1019 for these data can be found in section Table 1.

1020

1021 **Author contributions**

1022 HZ, RL and PR designed the study. HZ and RL conducted the model development and  
1023 simulation experiments. PR, KV, PC, VN, BG and WY provided critical contribution to the  
1024 model development and the design of simulation experiments. HZ conducted the model  
1025 calibration, validation and the data analysis. RL, PR, PC, KV and BG provided support on  
1026 collecting forcing and validation data. HZ, RL and PR wrote the manuscript. All authors  
1027 contributed to interpretation and discussion of results and improved the manuscript.

1028

1029 **Competing interests**

1030 The contact author has declared that neither they nor their co-authors have any competing  
1031 interests.

1032

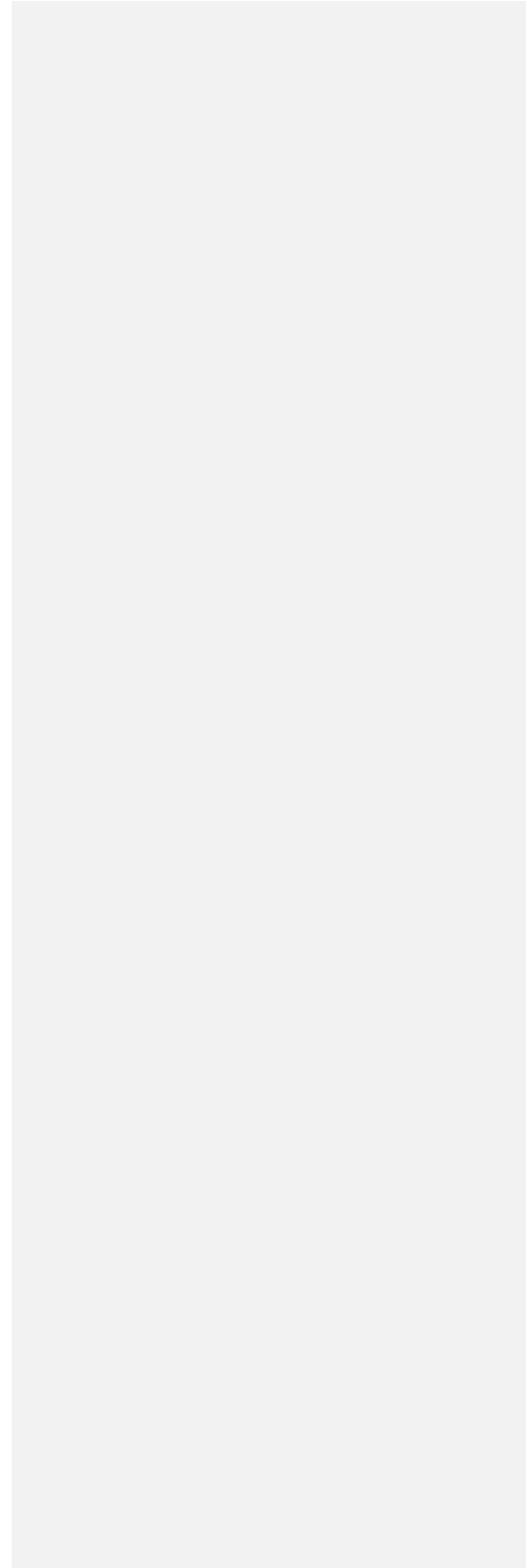
1033 **Acknowledgements**

1034 HZ and PR acknowledges the ‘Lateral-CNP’ project (No. 34823748) supported by the Fonds de  
1035 la Recherche Scientifique –FNRS and the VERIFY project that received funding from the  
1036 European Union’s Horizon 2020 research and innovation program under grant agreement No.  
1037 776810. RL and PC acknowledge funding by the French state aid managed by the ANR under  
1038 the "Investissements d'avenir" programme [ANR-16-CONV-0003\_Cland]. P.R. received funding  
1039 from the European Union’s Horizon 2020 research and innovation programme under Grant  
1040 Agreement no. 101003536 (ESM2025 – Earth System Models for the Future).

1041

1042

45



1043 **References:**

- 1044 Abotalib, A. Z., and Mohamed, R. S. A.: Surface evidences supporting a probable new concept for the river systems  
1045 evolution in Egypt: a remote sensing overview. *Environ. Earth Sci.*, 69, 1621-1635, 2012.
- 1046 Abrams, M., Crippen, R., and Fujisada, H.: ASTER Global Digital Elevation Model (GDEM) and ASTER Global  
1047 Water Body Dataset (ASTWBD). *Remote Sens.*, 12, 2020.
- 1048 Abril, G., Nogueira, M., Etcheber, H., Cabecadas, G., Lemaire, E., and Brogueira, M. J.: Behaviour of organic  
1049 carbon in nine contrasting European estuaries. *Estuar., Coast. Shelf Sci.*, 54, 241-262, 2002.
- 1050 Arnold, J. G., Williams, J. R., and Maidment, D. R.: Continuous-time water and sediment-routing model for large  
1051 basins. *J. Hydraul. Eng.*, 121, 171-179, 1995.
- 1052 Bakker, M. M., Govers, G., and Rounsevell, M. D. A.: The crop productivity–erosion relationship: an analysis based  
1053 on experimental work. *Catena*, 57, 55-76, 2004.
- 1054 Battin, T. J., Luysaert, S., Kaplan, L. A., Aufdenkampe, A. K., Richter, A., and Tranvik, L. J.: The boundless  
1055 carbon cycle. *Nat. Geosci.*, 2, 598-600, 2009.
- 1056 Berhe, A. A., Harte, J., Harden, J. W., and Torn, M. S.: The Significance of the Erosion-induced Terrestrial Carbon  
1057 Sink. *BioScience*, 57, 337-346, 2007.
- 1058 Beusen, A. H. W., Dekkers, A. L. M., Bouwman, A. F., Ludwig, W., and Harrison, J.: Estimation of global river  
1059 transport of sediments and associated particulate C, N, and P. *Global Biogeochem. Cycles*, 19,  
1060 <https://doi.org/10.1029/2005GB002453>, 2005.
- 1061 Borrelli, P., Robinson, D. A., Fleischer, L. R., Lugato, E., Ballabio, C., Alewell, C., Meusburger, K., Modugno, S.,  
1062 Schütt, B., Ferro, V., Bagarello, V., Oost, K. V., Montanarella, L., and Panagos, P.: An assessment of the  
1063 global impact of 21st century land use change on soil erosion. *Nat. Commun.*, 8, 2017.
- 1064 Borrelli, P., Van Oost, K., Meusburger, K., Alewell, C., Lugato, E., and Panagos, P.: A step towards a holistic  
1065 assessment of soil degradation in Europe: Coupling on-site erosion with sediment transfer and carbon fluxes.  
1066 *Environ. Res.*, 161, 291-298, 2018.
- 1067 Caffrey, J. M., Coloern, J. E., and Grenz, C.: Changes in production and respiration during a spring phytoplankton  
1068 bloom in San Francisco Bay, California, USA: implications for net ecosystem metabolism. *Mar. Ecol. Prog.  
1069 Ser.*, 172, 1-12, 1998.
- 1070 Camino-Serrano, M., Guenet, B., Luysaert, S., Ciais, P., Bastrikov, V., De Vos, B., Gielen, B., Gleixner, G., Jorret-  
1071 Puig, A., Kaiser, K., Kothawala, D., Lauerwald, R., Peñuelas, J., Schrumppf, M., Vicca, S., Vuichard, N.,  
1072 Walmsley, D., and Janssens, I. A.: ORCHIDEE-SOM: modeling soil organic carbon (SOC) and dissolved  
1073 organic carbon (DOC) dynamics along vertical soil profiles in Europe. *Geosci. Model Dev.*, 11, 937-957, 2018.
- 1074 Campoy, A., Ducharme, A., Cheruy, F., Hourdin, F., Polcher, J., and Dupont, J. C.: Response of land surface fluxes  
1075 and precipitation to different soil bottom hydrological conditions in a general circulation model. *J. Geophys.  
1076 Res.: Atmos.*, 118, 725-710,739, 2013.
- 1077 Castro, J. M., and Thorne, C. R.: The stream evolution triangle: Integrating geology, hydrology, and biology. *River  
1078 Res. Appl.*, 35, 315-326, 2019.
- 1079 Chaplot, V. A. M., Rumpel, C., and Valentin, C.: Water erosion impact on soil and carbon redistributions within

1080 uplands of Mekong River. *Global Biogeochem. Cycles*, 19, GB4004, 2005.

1081 Chappell, A., Baldock, J., and Sanderman, J.: The global significance of omitting soil erosion from soil organic  
1082 carbon cycling schemes. *Nat. Clim. Chang.*, 6, 187-191, 2016.

1083 Chini, L. P., Hurr, G. C., and Frohling, S.: Harmonized Global Land Use for Years 1500 – 2100, V1. Data set.  
1084 Available on-line [<http://daac.ornl.gov>] from Oak Ridge National Laboratory Distributed Active Archive  
1085 Center, Oak Ridge, Tennessee, USA, <http://dx.doi.org/10.3334/ORNLDAAC/1248>, 2014.

1086 Ciais, P., Sabine, C., Bala, G., Bopp, L., Brovkin, V., Canadell, J., Chhabra, A., DeFries, R., Galloway, J., Heimann,  
1087 M., Jones, C., Le Quéré, C., Myneni, R. B., Piao, S. L., and Thornton, P.: Carbon and Other Biogeochemical  
1088 Cycles, in: Stocker, T. F., Qin, D., Plattner, G.-K., Tignor, M., Allen, S. K., Boschung, J., Nauels, A., Xia, Y.,  
1089 Bex, V., and Midgley, P. M. (Eds.), *Climate Change 2013: The Physical Science Basis. Contribution of*  
1090 *Working Group I to the Fifth Assessment Report of the Intergovernmental Panel on Climate Change*  
1091 Cambridge University Press, Cambridge, United Kingdom and New York, NY, USA, 2013.

1092 Ciais, P., Yao, Y., Gasser, T., Baccini, A., Wang, Y., Lauerwald, R., Peng, S., Bastos, A., Li, W., Raymond, P. A.,  
1093 Canadell, J. G., Peters, G. P., Andres, R. J., Chang, J., Yue, C., Dolman, A. J., Haverd, V., Hartmann, J.,  
1094 Laruelle, G., Konings, A. G., King, A. W., Liu, Y., Luysaert, S., Maignan, F., Patra, P. K., Pregon, A.,  
1095 Regnier, P., Pongratz, J., Poulter, B., Shvidenko, A., Valentini, R., Wang, R., Broquet, G., Yin, Y.,  
1096 Zscheischler, J., Guenet, B., Goll, D. S., Ballantyne, A. P., Yang, H., Qiu, C., and Zhu, D.: Empirical estimates  
1097 of regional carbon budgets imply reduced global soil heterotrophic respiration. *Natl. Sci. Rev.*, 8,  
1098 <https://doi.org/10.1093/nsr/nwaa145>, 2021.

1099 Cohen, S., Kettner, A. J., and Syvitski, J. P. M.: Global suspended sediment and water discharge dynamics between  
1100 1960 and 2010: Continental trends and intra-basin sensitivity. *Glob. Planet. Change*, 115, 44-58, 2014.

1101 Cole, J. J., Prairie, Y. T., Caraco, N. F., McDowell, W. H., Tranvik, L. J., Striegl, R. G., Duarte, C. M., Kortelainen,  
1102 P., Downing, J. A., Middelburg, J. J., and Melack, J.: Plumbing the Global Carbon Cycle: Integrating Inland  
1103 Waters into the Terrestrial Carbon Budget. *Ecosystems*, 10, 172-185, 2007.

1104 Coulthard, T. J., and Van de Wiel, M. J.: Modelling river history and evolution. *Philosophical Transactions A*  
1105 *Mathematical, Phys. Eng. Sci.*, 370, 2123-2142, 2012.

1106 d'Orgeval, T., Polcher, J., and de Rosnay, P.: Sensitivity of the West African hydrological cycle in ORCHIDEE to  
1107 infiltration processes, *Hydrol. Earth Syst. Sci.*, 12, 1387-1401, <https://doi.org/10.5194/hess-12-1387-2008>,  
1108 2008.

1109 Dirmeyer, P. A., Gao, X., Zhao, M., Guo, Z., Oki, T., and Hanasaki, N.: GSWP-2: Multimodel Analysis and  
1110 Implications for Our Perception of the Land Surface. *Bull. Amer. Meteorol. Soc.*, 87, 1381-1398, 2006.

1111 Doetterl, S., Berhe, A. A., Nadeu, E., Wang, Z., Sommer, M., and Fiener, P.: Erosion, deposition and soil carbon: A  
1112 review of process-level controls, experimental tools and models to address C cycling in dynamic landscapes.  
1113 *Earth Sci. Rev.*, 154, 102-122, 2016.

1114 Drake, T. W., Raymond, P. A., and Spencer, R. G. M.: Terrestrial carbon inputs to inland waters: A current  
1115 synthesis of estimates and uncertainty. *Limn. Oceanogr. Lett.*, 3, 132-142, 2018.

1116 FAO/IIASA/ISRIC/ISSCAS/JRC: Harmonized World Soil Database (version 1.2), FAO, Rome, Italy and IIASA,

1117 Laxenburg, Austria, 2012.

1118 Galy, V., France-Lanord, C., and Lartiges, B.: Loading and fate of particulate organic carbon from the Himalaya to  
1119 the Ganga–Brahmaputra delta. *Geochim. Cosmochim. Acta*, 72, 1767-1787, 2008.

1120 Gassman, P. W., Sadeghi, A. M., and Srinivasan, R.: Applications of the SWAT Model Special Section: Overview  
1121 and Insights. *J. Environ. Qual.*, 43, 1-8, 2014.

1122 Gregorich, E. G., Greer, K. J., Anderson, D. W., and Liang, B. C.: Carbon distribution and losses: erosion and  
1123 deposition effects. *Soil Tillage Res.*, 47, 291-302, 1998.

1124 Guenet, B., Camino-Serrano, M., Ciais, P., Tifafi, M., Maignan, F., Soong, J. L., and Janssens, I. A.: Impact of  
1125 priming on global soil carbon stocks. *Glob. Change Biol.*, 24, 1873-1883, 2018.

1126 Guenet, B., Moyano, F. E., Peylin, P., Ciais, P., and Janssens, I. A.: (2016) Towards a representation of priming on  
1127 soil carbon decomposition in the global land biosphere model ORCHIDEE (version 1.9.5.2). *Geosci. Model  
1128 Dev.*, 9, 841-855, 2016.

1129 Guenet, B., Neill, C., Bardoux, G., and Abbadie, L.: Is there a linear relationship between priming effect intensity  
1130 and the amount of organic matter input? *Appl. Soil Ecol.*, 46, 436-442, 2010.

1131 Guimberteau, M., Drapeau, G., Ronchail, J., Sultan, B., Polcher, J., Martinez, J. M., Prigent, C., Guyot, J. L.,  
1132 Cochonneau, G., Espinoza, J. C., Filizola, N., Fraizy, P., Lavado, W., De Oliveira, E., Pombosa, R., Noriega,  
1133 L., and Vauchel, P.: Discharge simulation in the sub-basins of the Amazon using ORCHIDEE forced by new  
1134 datasets. *Hydrol. Earth Syst. Sci.*, 16, 911-935, 2012.

1135 Guimberteau, M., Zhu, D., Maignan, F., Huang, Y., Yue, C., Dantec-Nédélec, S., Ottlé, C., Jornet-Puig, A., Bastos,  
1136 A., Laurent, P., Goll, D., Bowring, S., Chang, J., Guenet, B., Tifafi, M., Peng, S., Krinner, G., Ducharne, A.,  
1137 Wang, F., Wang, T., Wang, X., Wang, Y., Yin, Z., Lauerwald, R., Joetzier, E., Qiu, C., Kim, H., and Ciais, P.:  
1138 ORCHIDEE-MICT (revision 4126), a land surface model for the high-latitudes: model description and  
1139 validation. *Geosci. Model Dev.*, 11, 121-163, 2018.

1140 [Habersack, H., Hein, T., Stanica, A., Liska, I., Mair, R., Jager, E., Hauer, C. and Bradley, C.: Challenges of river  
1141 basin management: Current status of, and prospects for, the River Danube from a river engineering perspective.  
1142 \*Sci. Total Environ.\*, 543, 828-845, 2016.](#)

1143 Hanson, P. C., Hamilton, D. P., Stanley, E. H., Preston, N., Langman, O. C., and Kara, E. L.: Fate of allochthonous  
1144 dissolved organic carbon in lakes: a quantitative approach. *PLoS One*, 6, e21884, 2011.

1145 Haregeweyn, N., Poesen, J., Deckers, J., Nyssen, J., Haile, M., Govers, G., Verstraeten, G., and Moeyersons, J.:  
1146 Sediment-bound nutrient export from micro-dam catchments in Northern Ethiopia. *Land Degrad. Dev.*, 19,  
1147 136-152, 2008.

1148 Hartmann, J., Lauerwald, R., and Moosdorf, N.: GLORICH - Global river chemistry database, in: PANGAEA (Ed.),  
1149 2019.

1150 Hengl, T., de Jesus, J. M., MacMillan, R. A., Batjes, N. H., Heuvelink, G. B., Ribeiro, E., Samuel-Rosa, A.,  
1151 Kempen, B., Leenaars, J. G., Walsh, M. G., and Gonzalez, M. R.: SoilGrids1km--global soil information based  
1152 on automated mapping. *PLoS One*, 9, e105992, 2014.

1153 Hu, Y., Kuhn, N. J.: Erosion-induced exposure of SOC to mineralization in aggregated sediment. *Catena*, 137, 517-



1154 525, 2016.

1155 Hoffmann, T. O.: 9.20 - Carbon Sequestration on Floodplains, in: *Treatise on Geomorphology (Second Edition)*,  
1156 edited by: Shroder, J. F., Academic Press, Cambridge, Massachusetts, United States, 10, 458-477, 2022,  
1157 <https://doi.org/10.1016/B978-0-12-818234-5.00069-9>.

1158 Hoffmann, T. O., Baulig, Y., Fischer, H., and Blöthe, J.: Scale breaks of suspended sediment rating in large rivers in  
1159 Germany induced by organic matter. *Earth Surf. Dynam.*, 8, 661–678, 2020.

1160 Hoffmann, T., Schlummer, M., Notebaert B., Verstraeten, G., and Korup, O.: Carbon burial in soil sediments from  
1161 Holocene agricultural erosion, Central Europe. *Glob. Biogeochem. Cy.*, 27, 828-835, 2013.

1162 Janssens, I. A., Freibauer, A., Ciais, P., Smith, P., Nabuurs, G. J., Folberth, G., Schlamadinger, B., Hutjes, R. W.,  
1163 Ceulemans, R., Schulze, E. D., Valentini, R., and Dolman, A. J.: Europe's terrestrial biosphere absorbs 7 to  
1164 12% of European anthropogenic CO<sub>2</sub> emissions. *Science*, 300, 1538-1542, 2003.

1165 Jetten, V., Govers, G., Hessel, R.: Erosion models: quality of spatial predictions. *Hydrol. Process.*, 17, 887-900,  
1166 2003.

1167 Kalbitz, K., Schmerwitz, J., Schwesig, D., and Matzner, E.: Biodegradation of soil-derived dissolved organic matter  
1168 as related to its properties. *Geoderma*, 113, 273-291, 2003.

1169 Knapp, A. K., Briggs, J. M., and Koelliker, J. K.: Frequency and Extent of Water Limitation to Primary Production  
1170 in a Mesic Temperate Grassland. *Ecosystems*, 4, 19-28, 2001.

1171 Krinner, G., Viovy, N., de Noblet-Ducoudré, N., Ogée, J., Polcher, J., Friedlingstein, P., Ciais, P., Sitch, S., and  
1172 Prentice, I. C.: A dynamic global vegetation model for studies of the coupled atmosphere-biosphere system.  
1173 *Global Biogeochem. Cycles*, 19, 2005.

1174 Lal, R.: Soil erosion and the global carbon budget. *Environ. Int.*, 29, 437-450, 2003.

1175 Lal, R.: Soil carbon sequestration impacts on global climate change and food security. *Science*, 304, 1623-1627,  
1176 2004.

1177 Lauerwald, R., Laruelle, G., Hartmann, J., Ciais, P., and Regnier, P.: Spatial patterns in CO<sub>2</sub> evasion from the global  
1178 river network: Spatial pattern of riverine pCO<sub>2</sub> and FCO<sub>2</sub>. *Global Biogeochem. Cycles*, 29, 2015.

1179 Lauerwald, R., Regnier, P., Camino-Serrano, M., Guenet, B., Guimberteau, M., Ducharme, A., Polcher, J., and Ciais,  
1180 P.: ORCHILEAK (revision 3875): a new model branch to simulate carbon transfers along the terrestrial–  
1181 aquatic continuum of the Amazon basin. *Geosci. Model Dev.*, 10, 3821-3859, 2017.

1182 Lauerwald, R., Regnier, P., Guenet, B., Friedlingstein, P., and Ciais, P.: How Simulations of the Land Carbon Sink  
1183 Are Biased by Ignoring Fluvial Carbon Transfers: A Case Study for the Amazon Basin. *One Earth*, 3, 226-236,  
1184 2020.

1185 Lehner, B., Verdin, K., and Jarvis, A.: New global hydrography derived from spaceborne elevation data. *Eos*,  
1186 *Transactions, AGU*, 89, 93-94, 2008.

1187 Lugato, E., Paustian, K., Panagos, P., Jones, A., and Borrelli, P.: Quantifying the erosion effect on current carbon  
1188 budget of European agricultural soils at high spatial resolution. *Glob. Change Biol.*, 22, 1976-1984, 2016.

1189 Luo, X., Li, H., Leung L.R., Tesfä, T. K., Getirana, A., Papa, F., and Hess L. L.: Modeling surface water dynamics  
1190 in the Amazon Basin using MOSART-Inundation v1.0: impacts of geomorphological parameters and river flow

1191 representation. *Geosci. Model Dev.*, 10, 1233-1259, 2017.

1192 Maavara, T., Lauerwald, R., Regnier, P., and Van Cappellen, P.: Global perturbation of organic carbon cycling by  
1193 river damming. *Nat. Commun.*, 8, 15347, 2017.

1194 Mei, X., Van Gelder, P., Dai, Z., and Tang, Z.: Impact of dams on flood occurrence of selected rivers in the United  
1195 States. *Front. Earth Sci.*, 11, 268-282, 2016.

1196 Meybeck, M.: Riverine transport of atmospheric carbon: sources, global typology and budget. *Water Air Soil  
1197 Pollut.*, 70, 443-463, 1993.

1198 Molinas, A., and Wu, B.: Transport of sediment in large sand-bed rivers. *J. Hydraul. Res.*, 39, 135-146, 2001.

1199 Moore, I. D., and Wilson, J. P.: Length-slope factors for the Revised Universal Soil Loss Equation: Simplified  
1200 method of estimation. *J. Soil Water Conserv.*, 47, 423-428, 1992.

1201 Nadeu, E., de Vente, J., Martínez-Mena, M., and Boix-Fayos, C.: Exploring particle size distribution and organic  
1202 carbon pools mobilized by different erosion processes at the catchment scale. *J. Soils Sediments*, 11, 667-678,  
1203 2011.

1204 Naipal, V., Lauerwald, R., Ciais, P., Guenet, B., and Wang, Y.: CE-DYNAM (v1): a spatially explicit process-based  
1205 carbon erosion scheme for use in Earth system models. *Geosci. Model Dev.*, 13, 1201-1222, 2020.

1206 Nakhavali, M., Lauerwald, R., Regnier, P., Guenet, B., Chadburn, S., and Friedlingstein, P.: Leaching of dissolved  
1207 organic carbon from mineral soils plays a significant role in the terrestrial carbon balance. *Glob. Change Biol.*,  
1208 27, 1083-1096, 2021.

1209 Nardi, F., Annis, A., Di Baldassarre, G., Vivoni, E.R., and Grimaldi, S.: GFPLAIN250m, a global high-resolution  
1210 dataset of Earth's floodplains. *Sci. Data*, 6, 180309, 2019.

1211 Nearing, M. A., Foster, G. R., Lane, L. J., and Finkner, S. C.: A Process-Based Soil Erosion Model for USDA-  
1212 Water Erosion Prediction Project Technology. *Transactions of the Asae*, 32, 1587-1593, 1989.

1213 Neckles, H. A., and Neill, C.: Hydrologic control of litter decomposition in seasonally flooded prairie marshes.  
1214 *Hydrobiologia*, 286, 155-165, 1994.

1215 Neitsch, S. L., Williams, J. R., Arnold, J. G., and Kiniry, J. R.: Soil and Water Assessment Tool Theoretical  
1216 Documentation Version 2009. Texas Water Resources Institute, College Station, 2011.

1217 Nie, X., Li, Z., He, J., Huang, J., Zhang, Y., Huang, B., Ma, W., Lu, Y., and Zeng, G.: Enrichment of organic carbon  
1218 in sediment under field simulated rainfall experiments. *Environ. Earth Sci.*, 74, 5417-5425, 2015.

1219 Nodvin, S. C., Driscoll, C. T., and Likens, G. E.: Simple partitioning of anions and dissolved organic carbon in a  
1220 forest soil. *Soil Sci.*, 142, 27-35, 1986.

1221 Nunes, A. N., de Almeida, A. C., and Coelho, C. O. A.: (2011) Impacts of land use and cover type on runoff and soil  
1222 erosion in a marginal area of Portugal. *Appl. Geogr.*, 31, 687-699, 2011.

1223 Oeurng, C., Sauvage, S., and Sánchez-Pérez, J. M.: Assessment of hydrology, sediment and particulate organic  
1224 carbon yield in a large agricultural catchment using the SWAT model. *J. Hydrol.*, 401, 145-153, 2011.

1225 Parton, W. J., Schimel, D. S., Cole, C. V., and Ojima, D. S.: Analysis of Factors Controlling Soil Organic Matter  
1226 Levels in Great Plains Grasslands I. *Soil Sci. Soc. Am. J.*, 51, 1173-1179, 1987.

1227 Parton, W. J., Stewart, J. W. B., and Cole, C. V.: Dynamics of C, N, P and S in grassland soils: a model.

1228 Biogeochemistry, 5, 109-131, 1988.

1229 Polyakov, V. O., and Lal, R.: Soil organic matter and CO<sub>2</sub> emission as affected by water erosion on field runoff  
1230 plots. Geoderma, 143, 216-222, 2008.

1231 Quine, T. A.: An investigation of spatial variation in soil erosion, soil properties and crop production with an  
1232 agricultural field in Devon, UK. J. Soil Water Conserv., 57, 55-65, 2002.

1233 Quinton, J. N., Govers, G., Van Oost, K., and Bardgett, R. D.: The impact of agricultural soil erosion on  
1234 biogeochemical cycling. Nat. Geosci., 3, 311-314, 2010.

1235 Raymond, P. A., Hartmann, J., Lauerwald, R., Sobek, S., McDonald, C., Hoover, M., Butman, D., Striegl, R.,  
1236 Mayorga, E., Humborg, C., Kortelainen, P., Durr, H., Meybeck, M., Ciais, P., and Guth, P.: Global carbon  
1237 dioxide emissions from inland waters. Nature, 503, 355-359, 2013.

1238 Reddy, K. R., Patrick Jr, and W. H.: Effect of alternate aerobic and anaerobic conditions on redox potential, organic  
1239 matter decomposition and nitrogen loss in a flooded soil. Soil Biol. Biochem., 7, 87-94, 1975.

1240 Regnier, P., Friedlingstein, P., Ciais, P., Mackenzie, F. T., Gruber, N., Janssens, I. A., Laruelle, G. G., Lauerwald,  
1241 R., Luysaert, S., Andersson, A. J., Arndt, S., Arnosti, C., Borges, A. V., Dale, A. W., Gallego-Sala, A.,  
1242 Godd ris, Y., Goossens, N., Hartmann, J., Heinze, C., Ilyina, T., Joos, F., LaRowe, D. E., Leifeld, J., Meysman,  
1243 F. J. R., Munhoven, G., Raymond, P. A., Spahni, R., Suntharalingam, P., and Thullner, M.: Anthropogenic  
1244 perturbation of the carbon fluxes from land to ocean. Nat. Geosci., 6, 597-607, 2013.

1245 [Regnier, P., Resplandy, L., Najjar, R. G., and Ciais, P.: The land-to-ocean loops for the global carbon cycle. Nature,](#)  
1246 [603, 401-410, 2022.](#)

1247 Reynolds, C., Jackson, T., and Rawls, W.: Estimating available water content by linking the FAO soil map of the  
1248 world with global soil profile databases and pedo-transfer functions, Am. Geophys. Union Fall Meet. EOS  
1249 Trans. Spring Meet. Suppl., 80, S132, 1999.

1250 Sanderman, J., Hengl, T., and Fiske, G. J.: Soil carbon debt of 12,000 years of human land use. Proc. Natl. Acad.  
1251 Sci., 114, 9575-9580, 2017.

1252 Schneider, C., Fl rke, M., Eisner, E., and Voss, F.: Large scale modelling of bankfull flow: An example for Europe.  
1253 J. Hydrol., 408, 235-245, 2011.

1254 Shangguan, W., Dai, Y., Duan, Q., Liu, B., and Yuan, H.: A global soil data set for earth system modeling. J. Adv.  
1255 Model. Earth Syst., 6, 249-263, 2014.

1256 Sharpley, A. N., and Williams, J. R.: EPIC-erosion/productivity impact calculator: 2. User manual. Technical  
1257 Bulletin - United States Department of Agriculture, 4, 206-207, 1990.

1258 Smith, S. V., Renwick, W. H., Buddemeier, R. W., and Crossland, C.J.: Budgets of soil erosion and deposition for  
1259 sediments and sedimentary organic carbon across the conterminous United States. Global Biogeochem. Cycles,  
1260 15, 697-707, 2001.

1261 Stallard, R. F.: Terrestrial sedimentation and the carbon cycle: Coupling weathering and erosion to carbon burial.  
1262 Global Biogeochem. Cycles, 12, 231-257, 1998.

1263 Stocker, B. D., Zscheischler, J., Keenan, T. F., Prentice, I. C., Seneviratne, S. I., and Pe uelas, J.: Drought impacts  
1264 on terrestrial primary production underestimated by satellite monitoring. Nat. Geosci., 12, 264-270, 2019.

1265 Telmer, K., and Veizer, J.: Carbon fluxes, pCO<sub>2</sub> and substrate weathering in a large northern river basin, Canada:  
1266 carbon isotope perspectives. *Chem. Geol.*, 159, 61-86, 1999.

1267 Tian, H., Yang, Q., Najjar, R. G., Ren, W., Friedrichs, M. A. M., Hopkinson, C. S., and Pan, S.: Anthropogenic and  
1268 climatic influences on carbon fluxes from eastern North America to the Atlantic Ocean: A process-based  
1269 modeling study. *J. Geophys. Res.: Biogeosci.*, 120, 757-772, 2015.

1270 Timpe, K., and Kaplan, D.: The changing hydrology of a dammed Amazon. *Sci. Adv.*, 3, 11, e1700611, 2017.

1271 Van Hemelryck, H., Govers, G., Van Oost, K., and Merckx, R.: Evaluating the impact of soil redistribution on the in  
1272 situ mineralization of soil organic carbon. *Earth Surf. Process. Landf.*, 36, 427-438, 2011.

1273 Van Oost, K., Quine, T. A., Govers, G., De Gryze, S., Six, J., Harden, J. W., Ritchie, J. C., McCarty, G. W.,  
1274 Heckrath, G., Kosmas, C., Giraldez, J. V., da Silva, J. R., and Merckx, R.: The impact of agricultural soil  
1275 erosion on the global carbon cycle. *Science*, 318, 626-629, 2007.

1276 Vigiak, O., Malago, A., Bouraoui, F., Vanmaercke, M., Obreja, F., Poesen, J., Habersack, H., Feher, J., and Groselj,  
1277 S.: Modelling sediment fluxes in the Danube River Basin with SWAT. *Sci. Total Environ.*, 599-600, 992-1012,  
1278 2017.

1279 Vörösmarty, C. J., Fekete, B. M., Meybeck, M., and Lammers, R. B.: Geomorphometric attributes of the global  
1280 system of rivers at 30-minute spatial resolution. *J. Hydrol.*, 237, 17-39, 2000.

1281 Wang, X., Cammeraat, E. L., Romeijn, P., and Kalbitz, K.: Soil organic carbon redistribution by water erosion--the  
1282 role of CO<sub>2</sub> emissions for the carbon budget. *PLoS One*, 9, e96299, 2014a.

1283 Wang, Z., Govers, G., Steegen, A., Clymans, W., Van den Putte, A., Langhans, C., Merckx, R., and Van Oost, K.:  
1284 Catchment-scale carbon redistribution and delivery by water erosion in an intensively cultivated area.  
1285 *Geomorphology*, 124, 65-74, 2010.

1286 Wang, Z., Hoffmann, T., Six, J., Kaplan, J. O., Govers, G., Doetterl, S., and Van Oost, K.: Human-induced erosion  
1287 has offset one-third of carbon emissions from land cover change. *Nat. Clim. Chang.*, 7, 345-349, 2017.

1288 Wang, Z., Van Oost, K., and Govers, G.: Predicting the long-term fate of buried organic carbon in colluvial soils.  
1289 *Global Biogeochem. Cycles*, 29, 65-79, 2015.

1290 Wang, Z., Van Oost, K., Lang, A., Quine, T., Clymans, W., Merckx, R., Notebaert, B., and Govers, G.: The fate of  
1291 buried organic carbon in colluvial soils: a long-term perspective. *Biogeosciences*, 11, 873-883, 2014b.

1292 Xu, X., Sherry, R. A., Niu, S., Li, D., and Luo, Y.: Net primary productivity and rain-use efficiency as affected by  
1293 warming, altered precipitation, and clipping in a mixed-grass prairie. *Glob. Change Biol.*, 19, 2753-2764, 2013.

1294 Yamazaki, D., Kanae, S., Kim, H., and Oki T.: A physically based description of floodplain inundation dynamics in  
1295 a global river routing model. *Water Resour. Res.*, 47, W04501, doi:10.1029/2010WR009726, 2011.

1296 Zhang, H., Lauerwald, R., Regnier, P., Ciais, P., Yuan, W., Naipal, V., Guenet, B., Van Oost, K., and Camino-  
1297 Serrano, M.: Simulating Erosion-Induced Soil and Carbon Delivery From Uplands to Rivers in a Global Land  
1298 Surface Model. *J. Adv. Model. Earth Syst.*, 12, e2020MS002121, 2020.

1299 Zhang, H., Liu, S., Yuan, W., Dong, W., Xia, J., Cao, Y., and Jia, Y.: Loess Plateau check dams can potentially  
1300 sequester eroded soil organic carbon. *J. Geophys. Res. Biogeosci.*, 121, 2016.

1301 Zhang, H., Liu, S., Yuan, W., Dong, W., Ye, A., Xie, X., Chen, Y., Liu, D., Cai, W., and Mao, Y.: Inclusion of soil

1302 carbon lateral movement alters terrestrial carbon budget in China. *Sci. Rep.*, 4, 7247, 2014.